Lawrence Berkeley National Laboratory

Recent Work

Title

Identification of the strong Brønsted acid site in a metal-organic framework solid acid catalyst.

Permalink

https://escholarship.org/uc/item/4h95g09b

Journal

Nature chemistry, 11(2)

ISSN

1755-4330

Authors

Trickett, Christopher A
Osborn Popp, Thomas M
Su, Ji
et al.

Publication Date

2019-02-01

DOI

10.1038/s41557-018-0171-z

Peer reviewed

eScholarship.org Powered by the California Digital Library
University of California

Identification of the Strong Brønsted Acid Site in a Metal-Organic Framework Solid Acid Catalyst

Christopher A. Trickett,[1,2,†] Thomas M. Osborn Popp,[1,2,3†] Ji Su,[1,2] Chang Yan,[4] Jonathan Weisberg,[1] Ashfia Huq,[5] Philipp Urban,[1,2] Juncong Jiang,[1,2] Markus J. Kalmutzki,[1,2] Qingni Liu,[1,2] Jayeon Baek,[1,2] Martin P. Head-Gordon,[1] Gabor A. Somorjai,[1,2] Jeffrey A. Reimer,[2,3] and Omar M. Yaghi[1,2,*]

[1]Department of Chemistry, Kavli Energy NanoSciences Institute at Berkeley, and Berkeley Global Science Institute, University of California-Berkeley, Berkeley, California 94720

[2]Materials Sciences Division, Lawrence Berkeley National Laboratory, Berkeley, CA 94720

[3]Department of Chemical and Biomolecular Engineering, University of California, Berkeley, California 94720, USA University of California-Berkeley, Berkeley, California 94720

[4]Department of Chemistry, Stanford University, Stanford, CA 94305

[5]Neutron Scattering Division, Oak Ridge National Laboratory, P.O. Box 2008 MS-6475, Oak Ridge, TN 37831

[†]Authors contributed equally

[*]Correspondence to: yaghi@berkeley.edu

Abstract: It remains difficult to understand the surface of solid acid catalysts at the molecular level, despite their importance for industrial catalytic applications. A sulfated zirconium-based metal-organic framework, MOF-808-SO_4, has previously been shown to be a strong solid Brønsted acid material. In this report, we probe the origin of its acidity through an array of spectroscopic, crystallographic, and computational characterization techniques. The strongest Brønsted acid site is shown to consist of a specific arrangement of adsorbed water and sulfate moieties on the zirconium clusters. When a water molecule adsorbs to one zirconium atom, it participates in a hydrogen bond with a sulfate moiety that is chelated to a neighboring zirconium atom; this motif in turn results in the presence of a strongly acidic proton. On dehydration, the material loses its acidity. The hydrated sulfated MOF exhibits good catalytic performance for the dimerization of isobutene (2-methyl-1-propene), achieving 100% selectivity for C8 products with good conversion efficiency.

The chemistry at the surface of solid acid catalysts is of vital importance for industrial catalytic applications, yet a precise molecular picture of these surfaces remains elusive. Attempts to obtain a clear view of the Brønsted acid sites in solid acids such as sulfated zirconia have resulted in multiple proposed models, in part due to the difficulty in characterizing the structure of this

amorphous material, but also because of wildly variable properties depending on preparation conditions (1-11). Discerning the molecular structures responsible for the activity of solid acid catalysts provides a richer perspective on the functional properties and catalytic mechanisms of these materials, and illuminates the fundamental surface chemistry relating the molecular structures and their functions. Recently, the synthesis of a metal-organic framework (MOF) solid acid catalyst was reported, achieved by treating a Zr-based MOF, MOF-808, with sulfuric acid to yield the solid acid MOF, MOF-808-SO_4, which was shown to be capable of performing several acid-catalyzed reactions (12,13). In this report, we conclusively identify the structure of the strong Brønsted acid site in MOF-808-SO_4, as being a hydrogen bond pair of two species, water and chelating sulfate, adsorbed on the surface of its zirconium clusters, where the acidic proton is arises as a result of the hydrogen bond. We achieve this through a union of crystallographic, spectroscopic, and computational studies. We also show that MOF-808-SO_4 exhibits good activity and selectivity for the dimerization of isobutene to isooctene, and that dehydration of the material significantly reduces the catalytic activity, confirming the role of water as necessary to the strong acidity of the site.

Results and Discussion

The preparation of MOF-808-SO_4 was performed by first synthesizing pristine MOF-808 (Fig. 1a), $Zr_6O_5(OH)_3(BTC)_2(HCOO)_5(OH_2)_2$, with a subsequent exchange of the formate ions on the zirconium clusters for sulfate ions simply by washing the MOF in dilute sulfuric acid (12). The MOF-808 backbone is comprised of an octahedron of zirconium atoms that are triply bridged by μ^3-O and μ^3-OH groups. The formate groups in the pristine structure each bridge two zirconium atoms to form a six-membered belt around the cluster (13). One cluster is connected to six other clusters through benzene tricarboxylate (BTC) linkers, three above and three below the belt of formates, resulting in a framework with spn topology. Once the formate ions are exchanged for sulfate to yield MOF-808-SO_4 (Fig. 1b), these sulfates may take on multiple binding modes and can take one of several positions along the belt interspersed between additional ligated water molecules, resulting in long-range disorder from one cluster to the next. As this disorder is confined to the surface species on the zirconium clusters, the surface of each cluster has a slightly different local molecular 'decoration,' (Fig. 1c) while the structural backbone of MOF-808 is still conserved throughout (14-17). Our challenge is to understand the molecular decoration of the zirconium clusters in MOF-808-SO_4 by first identifying the structures that decorate the cluster surface, and from there, discerning which arrangement of decorating structures results in a strong Brønsted acid site.

Understanding the molecular decoration of the zirconium clusters

Elucidating the coordination mode of sulfate is essential for discerning the local structures that exist on the surface of the clusters. From single crystal X-ray diffraction (SXRD) analysis of a crystal in aqueous solution, the sulfate groups are found to be coordinated in both a bridging and chelating mode (Supplementary Fig. 1), with the bridging mode dominating in a 4:1 ratio over chelating (Supplementary Section 3). To obtain further insight into what factors control the coordination mode of these ions, selenated MOF-808 (MOF-808-SeO_4) was synthesized in a similar manner to sulfated MOF-808. The MOF-808-SeO_4 framework in aqueous solution was found to possess only one coordination mode for selenate, where selenate bridges two zirconium atoms, suggesting that perhaps the increased atomic radius of selenium

enforces the bridging coordination mode. However, upon activation of these two MOFs under dynamic vacuum and heating at 120 ºC, both sulfate and selenate were found to have shifted into the chelating mode exclusively. This was confirmed using Rietveld refinement of the samples measured by powder X-ray diffraction (PXRD) in an argon atmosphere. The solid acid nature of MOF-808-SO_4 is only observed following activation at 120 °C, suggesting that the chelating coordination mode of sulfate is a key contributor to its catalytic activity.

Quantifying the average molecular formula for MOF-808-SO_4 constrains further the possibilities for ligand disorder on the surface of the zirconium clusters. Here, balancing the charge on the zirconium clusters guides our stoichiometric analysis. Using inductively coupled plasma-optical emission spectroscopy for elemental analysis, 2.3 sulfur atoms per 6 zirconium atoms were found, meaning an average of 2.3 sulfate groups per zirconium cluster. Since each zirconium atom is in the +4 oxidation state, there is an excess of positive charge that is not properly accounted for within the model so far. To probe this, we turned to powder neutron diffraction (PND) to obtain more precise information on the occupancies and thermal ellipsoids of light elements within the framework (Fig. 2a). A sample of MOF-808-SO_4 with deuterated BTC linker was measured at 10 K and 300 K and refined simultaneously against a structure model, revealing a 1:1 ratio of μ^3-O to μ^3-OH in both independent crystallographic positions within two standard deviations (Supplementary Section 2). An excess of μ^3-O is therefore not what balances the excess positive charge. There is substantially more electron density located around the position of the oxygen that connects zirconium to sulfur, O6, which is the same location as coordinated water molecules bound to the cluster in the as-synthesized MOF-808-SO_4. It is noteworthy to mention that the sulfate position could not be located by PND due to the low occupancy and extremely weak neutron scattering factor of sulfur, thus information from PXRD was used in combination with elemental analysis to confirm its presence in this sample.

As the only electron density unaccounted for in this model is located at position O6, where water is present in the structure prior to activation, we can infer that balance of the excess positive charge is achieved here by terminal hydroxide, produced by the deprotonation of water molecules. This assumption is plausible considering terminal water molecules bound to zirconium hydroxide clusters have been found to be acidic (18, 19). The position thus accounts for crystallographically superimposed oxygen from sulfate groups, hydroxide and water molecules that were not removed during the activation process. This overlap excludes the possibility of determining the precise coordinates of hydroxide, water and sulfate oxygen, but the total occupancy of these species was refined freely, converging to 78.4 ±1.1%. This corresponds to 9.4 oxygen atoms per cluster, out of a possible 12. Since there must be 4.6 oxygen atoms from 2.3 bidentate sulfate groups as found by elemental analysis, and 1.4 hydroxide groups for charge-balancing, this leaves 3.4 ± 0.1 oxygen atoms unaccounted for, and are assigned to ligated water. This was confirmed by thermogravimetric analysis - mass spectrometry (TGA-MS) on the activated sample, which demonstrated the loss of 3.1 water molecules per cluster prior to structure decomposition (Supplementary Fig. 16). The first water signal observed from the mass spectrometer peaked at 143 °C, and indicates water is still present following evacuation and heating. After a small, second water loss event at 236 ºC, the structure decomposes at around 350 °C. This trend can be explained by considering that losing neutral, terminal water ligands would not collapse the structure, but once the framework is completely dehydrated any further mass loss leads to structure decomposition, as this involves the loss of charged species. Evidence from elemental analysis, PND, ^{1}H nuclear magnetic resonance (NMR) of the digested MOF and TGA-

MS, lead to the average molecular formula of $Zr_6O_4(OH)_4(BTC)_2(SO_4)_{2.3}(OH)_{1.4}(OH_2)_{3.1}(DMF)_{0.4}$ for the activated form of MOF-808-SO_4.

Identifying the strong Brønsted acid site

With the average chemical formula now known, the possible species that decorate each zirconium cluster are constrained, simplifying the task of identifying the Brønsted acid site in MOF-808-SO_4. The potential acidic sources are discussed in turn. Firstly, terminal hydroxide may be eliminated simply because terminal water is present and bound to the cluster in the same manner as hydroxide, with terminal water being known to be more acidic (17,18). Protons on sulfate can also be ruled out since the pH of the solution when the MOF is washed with water following incorporation of sulfate is 3.5, while the pK_{a2} value of sulfuric acid is 1.92 (20). Therefore, sulfate must be fully deprotonated at this stage. A direct comparison between μ^3-OH and terminal water is not as straightforward; however, we found that the water molecules bound to the framework could be successfully removed by holding the temperature at 220 °C overnight while maintaining crystallinity and porosity. This sample will be hereafter referred to as dehydrated MOF-808-SO_4. If the water molecules are indeed the most acidic species present, the material should lose its strong acid properties upon dehydration.

To determine if water molecules are the source of the most acidic protons, we adsorbed trimethylphosphine oxide (TMPO) into MOF-808-SO_4 as a probe of acidity and performed ^{31}P solid state NMR with magic angle spinning (MAS). TMPO interacts with Brønsted and Lewis acid sites via the lone pairs on its oxygen atom. Strong acid sites polarize the phosphorus-oxygen bond, resulting in a linear relationship between ^{31}P chemical shift values of adsorbed TMPO and the strength of the acid site, where a higher ^{31}P chemical shift corresponds to a stronger acid site (21-25). MOF-808-SO_4 with adsorbed TMPO shows a ^{31}P resonance at 69 ppm associated with a strongly acidic site (Fig. 2b, i), consistent with what has been previously observed for this material (12). This resonance at 69 ppm is found to be absent when TMPO is used in dehydrated MOF-808-SO_4 (Fig. 2b, ii). As the loss of a water molecule is associated with the loss of the strongest acid site, this result supports the role of terminal water as the strongest Brønsted acid source.

At this point, two key molecular features decorating the zirconium clusters have been identified as essential to the acidity of MOF-808-SO_4: the chelating mode of sulfate and terminal water ligand. In isolation, neither of these two species is sufficient to account for the acidity of this MOF, therefore its strong Brønsted acidity must arise from a specific arrangement of these species on the cluster surface. Given the many possible ways to decorate the belt of the cluster with terminal water, terminal hydroxide, and chelating sulfate, several arrangements were chosen to be modeled and geometrically optimized using density functional theory (DFT). The formula $Zr_6O_4(OH)_4(C_2H_3O_2)_6(SO_4)_2(OH)_2(OH_2)_x$ was used as a representation of an average cluster, where x = 2 or 3. The restrictions on structural arrangement of the cluster included (i) the core $[Zr_6O_4(OH)_4(C_2H_3O_2)_6]^{6+}$ being fixed, with μ^3-O and –OH groups arranged in the commonly reported alternating arrangement to minimize charge repulsion, (ii) modeling sulfate as chelating to zirconium as opposed to bridging, (iii) using terminal hydroxide to charge-balance the cluster, (iv) including two to three water molecules per cluster. Additionally, individual clusters were modeled by truncating the linker with acetate groups, which assumes the clusters are electronically decoupled. The most enlightening result obtained from the different modeled arrangements on the clusters is from the comparison of terminal water in isolation versus adjacent to a chelating sulfate group. An O-H bond length of 0.98 Å was observed on the

terminal water molecules that have no significant interactions with neighboring adsorbed molecules. However, when the terminal water molecule is adjacent to chelating sulfate, there is a strong hydrogen bonding interaction, with an O-H bond length ranging from 1.02 – 1.05 Å depending on the particular cluster modeled, significantly longer than the O-H bond with no hydrogen bonding. This is accompanied by an O-H···O angle of 163-166° and a short H···O hydrogen bonding distance of 1.50 – 1.66 Å, indicating that the proton is very weakly bound. Indeed, the system can be viewed as a protonated conjugate of an adsorbed pair of hydroxide and sulfate, with the proton sitting between the two groups but localized mostly on the hydroxide. One example of this site on a modeled cluster is represented in Fig. 3, which was modeled with overall two water molecules and two chelating sulfate groups located on opposite sides of the zirconium cluster.

The broken symmetry of the water molecule at this proposed acid site implies that the water participating in a hydrogen bond to chelating sulfate should have distinctly different spectroscopic signatures for its two proton environments. We will refer to these two sites as H_a for the acidic proton on water participating in the hydrogen bond to chelating sulfate, and H_b for the other proton pointing into free space. To probe these proton chemical environments directly, we performed ^{1}H solid state NMR. Fig. 4a shows the ^{1}H MAS spectrum of MOF-808-SO_4 at 6 kHz MAS taken before and after dehydration, and their difference. The difference spectrum shows that two peaks at around 2.5 ppm and 8.1 ppm are lost as a result of dehydration. Assigning the identity of these resonances is informed by comparing to the DFT-calculated ^{1}H NMR chemical shifts of two of the modeled zirconium clusters (Section S7, Tables S4 and S5). The difference in chemical shift ($\Delta\delta$) between the H_a and H_b protons in the acid site is calculated for two cases to be $\Delta\delta$ = 5.1 ppm and $\Delta\delta$ = 9.1 ppm. Water lacking a strong hydrogen bonding interaction to chelating sulfate is calculated to have only $\Delta\delta$ = 2.0 ppm between the two protons. The changes in the spectra in Fig. 4a after dehydration suggest that the two lost resonances belong to the H_a and H_b protons on the water molecule in the acid site with $\Delta\delta$ = 5.6 ppm, where H_a, the acidic proton, is the downfield resonance.

In order to confirm that these two resonances are the H_a and H_b protons belonging to the same water molecule, a rotor-synchronized double-quantum (DQ) MAS NMR experiment with the back-to-back (BABA) recoupling sequence was performed. This experiment correlates proton resonances in the standard, single-quantum (SQ) spectrum by their proximity to one another through space. A peak in the DQ dimension indicates that a pair of protons is in close enough proximity to generate a double quantum coherence (26). As the closest pairs of protons in MOF-808-SO_4 belong to those on μ^1-water molecules, we expect these to be the primary coherences observed. The intensity of these peaks is dependent upon the number of duplicate pairs exhibiting this coherence, as well as the efficiency at which this coherence is excited, i.e. the internuclear distance (27). The SQ H_a and H_b resonances at 8.7 ppm 2.5 ppm, respectively, exhibit strong cross peaks at a DQ frequency of 11.2 ppm, indicating their close spatial proximity and confirming that these two resonances must arise from a single water species (Fig. 4b). The low-intensity cross peaks between 8.7 and 3.1 ppm may arise from a small subset of H_a and H_b protons in acid sites with a slightly different local arrangement of nearest neighbor μ^1-OH and μ^3-OH groups. Along the diagonal, a strong autocorrelation DQ peak at around 5.0 ppm is observed for an SQ resonance at around 2.5 ppm, which arises from pairs of protons belonging to isolated terminal water at other sites on the zirconium cluster. The chemical environment of the protons on water molecules not neighboring a chelating sulfate is similar to the chemical environment of the H_b proton in the acid site, and accordingly, their chemical shifts should be

similar. This is supported by our DFT calculations, where the chemical shifts of protons in these environments were calculated to be within about ± 1 ppm of one another. The ^{1}H solid state NMR results reveal a picture consistent with the proposed molecular conformation of the Brønsted acid site, where water hydrogen-bonded to sulfate has two protons with inequivalent O-H bond lengths and inequivalent chemical shifts. The subsequent loss of these peaks after dehydration at 220 °C is correlated with a loss of acidity, resulting in the conclusion that the strong Brønsted acid site arises from this hydrogen bonding interaction between water and chelating sulfate.

Removal of water at the acid site impacts catalytic performance

These results suggest a structure-property relationship in MOF-808-SO_4, where water must be present and adjacent to chelating sulfate to yield strong acidity. We sought to test this hypothesis by measuring the activity of MOF-808-SO_4 in catalyzing the dimerization of isobutene (2-methylprop-1-ene), and to see whether removing the water molecule in the active site by dehydration would affect this activity. The dimerization of isobutene may yield two products, either 2,4,4-trimethyl-1-pentene or 2,4,4-trimethyl-2-pentene, both referred to as isooctene (Fig. 5a). The terminal alkene product is prized as a starting material for synthesizing terminal aldehydes and alcohols, but both alkene products may be hydrogenated to form 2,4,4-trimethylpentane, known as isooctane, a valuable gasoline octane booster (28-30). In the process of dimerizing isobutene, higher order alkene oligomer products greater than C8 may form, which is typically disfavored, as a separation step is required to isolate the C8 species. Selectivity for C8 products is crucial if isooctane is the desired product (31,32). To that end, MOF-808-SO_4 was benchmarked against other solid acid catalysts for C8 selectivity and conversion efficiency (sulfated zirconia, Amberlyst, and H-ZSM-5) using a continuous gas flow setup, with isobutene diluted in helium and at atmospheric pressure (Supplementary Section 11). The advantage of using a gas flow setup over a solvent-based process is that it allows for continuous production, and negates the need to purify isooctene from solvent mixtures. Our benchmark materials were chosen based on their capacity to operate under these conditions, and their catalytic activities were evaluated with respect to the mass of the catalyst. MOF-808-SO_4 was found to be active even at room temperature, with conversion peaking at 160 °C at 21.5%, outperforming Amberlyst, sulfated zirconia and H-ZSM-5 under these conditions (Fig. 5b). The C8 selectivity of MOF-808-SO_4 is found to be 100% at 80 °C and lower, yet remains at 92.8% at 160 ºC, similar to sulfated zirconia (Fig. 5c). The C8 product distribution for both MOF-808-SO_4 and sulfated zirconia runs about 4:1 in favor of the terminal alkene product (Supplementary Figs. 28-30). H-ZSM-5 and Amberlyst exhibit C8 selectivity under 35% at all temperatures, forming a mixture of many different higher order oligomers. Though the C8 selectivity and product distribution for MOF-808-SO_4 and sulfated zirconia are comparable, under longer experiments of up to 15 days at 80 °C, MOF-808-SO_4 does not lose activity or selectivity, maintaining a constant 15% conversion while the conversion efficiency of sulfated zirconia drops by around 60% from its starting value of 5.2% (Fig. 5d). MOF-808-SO_4 does begin lose activity at 120 °C and 160 °C, and at a faster rate with increasing temperature, consistent with the notion that desorption of water from the zirconium clusters at higher temperatures should affect the Brønsted acid site. Indeed, when dehydrated MOF-808-SO_4 was tested as a catalyst, the conversion was found to be 80 % less than that of MOF-808-SO_4 at 80 °C (Fig. 5b). The great majority of the catalytic activity of the material can thus be attributed to this acid site, where water is adjacent and hydrogen bonded to chelating sulfate. The C8 selectivity and product

distribution for dehydrated MOF-808-SO_4 are almost identical to that of MOF-808-SO_4 and sulfated zirconia, indicating that this acid site alone is not responsible for the selectivity.

We conclude that perturbing the strong Brønsted acid site by removing the water adjacent to chelating sulfate has a significant negative impact on the catalytic performance of MOF-808-SO_4. The remaining activity of the material in the absence of this water molecule suggests that Lewis acid sites in the material may also contribute to its activity but to a lesser extent, a possibility supported by the observation of open metal sites in the PND refinement of the structure (Supplementary Section 2). Regeneration of the catalyst thus only requires replacing the water molecule adjacent to sulfate, which can be done by repeating the solvent exchange and activation process. Future work may find a more efficient process whereby the catalyst is regenerated continuously during operation by the addition of water vapor into the product stream, maintaining the active site even at higher temperatures.

The relative strength of this acid site compared to other acids is of interest, as its structure may serve as a model for the design of new strong acid sites. While MOF-808-SO_4 has been previously stated to be superacidic by colorimetric methods (12), these methods can sometimes prove unreliable for acid sites existing at the interface of the solid and gas phase (33). We can provide a thermodynamically-based estimate of the acidity of this specific Brønsted acid site based on a previously calculated relationship between the ^{31}P chemical shift of adsorbed TMPO and the deprotonation energy of simulated Brønsted acid sites (20,21). The TMPO resonance at 69 ppm correlated to the acid site in this material corresponds to a deprotonation energy of 1214 kJ/mol. It is generally accepted that a superacid is a medium in which the chemical potential of the proton is higher than in sulfuric acid (34). The deprotonation energy for gas-phase sulfuric acid has been experimentally determined to be 1295 kJ/mol (35), which suggests that this Brønsted site in MOF-808-SO_4 is at the very least comparable to sulfuric acid, and may even be considered superacidic by this measure. At its core, the structure of this site in MOF-808-SO_4 is characterized by the pairing of two bases (chelating sulfate and μ^1-OH) supported on two neighboring zirconium atoms and sharing a weakly bound proton between them. Thus such a Brønsted acid site construct may be quite generalizable, as it may be possible to reduce the deprotonation energy of this proton to yield even stronger acidity by manipulating the identities of these two bases or of the support atoms.

Data availability. Synthetic and experimental procedures, as well as crystallographic, spectroscopic and computational data are provided in the Supplementary Information. All other data are available from the authors upon reasonable request.

References

1. Arata, K. Solid Superacids. *Adv. Catal.* **37**, 165 (1990).
2. Ward, D. A. & Ko, E. I. One-Step Synthesis and Characterization of Zirconia-Sulfate Aerogels as Solid Superacids. *J. Catal.* **150,** 18–33 (1994).
3. Haase, F. & Sauer, J. The Surface Structure of Sulfated Zirconia: Periodic ab Initio Study of Sulfuric Acid Adsorbed on ZrO_2(101) and ZrO_2(001). *J. Am. Chem. Soc.* **120**, 13503–13512 (1998).
4. Bensitel, M., Saur, O., Lavalley, J.C., & Morrow, B. A. An infrared study of sulfated

zirconia. *Mater. Chem. Phys.* **19**, 147–156 (1988).

5. Clearfield, A., Serrette, G. P. D., & Khazi-Syed, A. H. Nature of hydrous zirconia and sulfated hydrous zirconia. *Catal. Today*. **20**, 295–312 (1994).

6. Kustov, L. M., Kazansky, V. B., Figueras, F., & Tichit, D. Investigation of the Acidic Properties of ZrO_2 Modified by SO_4^{2-} Anions. *J. Catal.* **150,** 143–149 (1994).

7. Adeeva, V. et al. Acid sites in sulfated and metal-promoted zirconium dioxide catalysts. *J. Catal.* **151**, 364–372 (1995).

8. Bolis, V., Magnacca, G., Cerrato, G., & Morterra, C., Microcalorimetric characterization of structural and chemical heterogeneity of superacid SO_4/ZrO_2 systems. *Langmuir*. **13**, 888–894 (1997).

9. Hino, M., Kurashige, M., Matsuhashi, H., & Arata, K. The surface structure of sulfated zirconia: Studies of XPS and thermal analysis. *Thermochim. Acta*. **441**, 35–41 (2006).

10. Arata, K. Organic syntheses catalyzed by superacidic metal oxides: sulfated zirconia and related compounds. *Green Chem.* **11**, 1719–1728 (2009).

11. Yadav, G. D. & Nair, J. J. Sulfated zirconia and its modified versions as promising catalysts for industrial processes. *Microporous Mesoporous Mater.* **33**, 1–48 (1999).

12. Jiang, J. et al. Superacidity in Sulfated Metal − Organic Framework-808. *J. Am. Chem. Soc.* **136**, 12844–12847 (2014).

13. Furukawa, H. et al. Water adsorption in porous metal-organic frameworks and related materials. *J. Am. Chem. Soc.* **136**, 4369–81 (2014).

14. Osborn Popp, T. M. & Yaghi, O.M. Sequence-Dependent Materials. *Acc. Chem. Res.* **50**, 532–534 (2017).

15. Cairns, A. B. & Goodwin, A. L. Structural disorder in molecular framework materials. *Chem. Soc. Rev.* **42**, 4881–93 (2013).

16. Furukawa, H., Müller, U., & Yaghi, O. M. "Heterogeneity within order" in metal-organic frameworks. *Angew. Chem. Int. Ed.* **54**, 3417–3430 (2015).

17. Trickett, C. A. et al. Definitive molecular level characterization of defects in UiO-66 crystals. *Angew. Chem. Int. Ed.* **54**, 11162–11167 (2015).

18. Åberg, M. & Glaser, J. ^{17}O and ^{1}H NMR study of the tetranuclear hydroxo zirconium complex in aqueous solution. *Inorg. Chim. Acta*. **206**, 53–61 (1993).

19. Springborg, J. Hydroxo-Bridged Complexes of Chromium (III), Cobalt (III), Rhodium (III), and Iridium (III). *Adv. Inorg. Chem.* **32**, 55–169 (1988).

20. Hall, J. *Lab Manual for Zumdahl/Zumdahl's Chemistry*, p. 656, (2002).

21. Zheng, A., Zhang, H., Lu, X., Liu, S. B., & Deng, F. Theoretical predictions of ^{31}P NMR chemical shift threshold of trimethylphosphine oxide absorbed on solid acid catalysts. *J. Phys. Chem. B* **112**, 4496–4505 (2008).

22. Zheng, A. et al. ^{31}P Chemical Shift of Adsorbed Trialkylphosphine Oxides for Acidity Characterization of Solid Acids Catalysts. *J. Phys. Chem.* **112**, 7349–7356 (2008).

23. Zheng, A., Huang, S.J., Liu, S. B., & Deng, F. Acid properties of solid acid catalysts characterized by solid-state ^{31}P NMR of adsorbed phosphorous probe molecules. *Phys. Chem. Chem. Phys.* **13**, 14889 (2011).

24. Chen, W. H. et al. A solid-state NMR, FT-IR and TPD study on acid properties of sulfated and metal-promoted zirconia: Influence of promoter and sulfation treatment. *Catal. Today*. **116**, 111–120 (2006).

25. Lunsford, J. H., Sang, H., Campbell, S. M., Liang, C. H., & Anthony, R. G. An NMR study of acid sites on sulfated-zirconia catalysts using trimethylphosphine as a probe. *Catal. Letters*. **27**, 305–314 (1994).

26. Gottwald, J., Demco, D. E., Graf, R., & Spiess, H. W. High-resolution double-quantum NMR spectroscopy of homonuclear spin pairs and proton connectivities in solids. *Chem. Phys. Lett.* **243**, 314–323 (1995).

27. Schnell, I., Brown, S. P., Low, H. Y., Ishida, H., & Spiess, H. W. An investigation of hydrogen bonding in benzoxazine dimers by fast magic-angle spinning and double-quantum ^{1}H NMR spectroscopy. *J. Am. Chem. Soc.* **120**, 11784–11795 (1998).

28. Mahdi, H. I. & Muraza, O. Conversion of isobutylene to octane-booster compounds after methyl tert-butyl ether phaseout: The role of heterogeneous catalysis. *Ind. Eng. Chem. Res.* **55**, 11193–11210 (2016).

29. Takahashi, K., Yamashita, M., & Nozaki, K. Tandem hydroformylation/hydrogenation of alkenes to normal alcohols using Rh/Ru dual catalyst or Ru single component catalyst. *J. Am. Chem. Soc.* **134**, 18746–18757 (2012).

30. Behr, A. *Ullman's Encyclopedia of Industrial Chemistry.* 223–269 (2010).

31. Izquierdo, J. F., Vila, M., Tejero, J., Cunill, F., & Iborra, M., Kinetic study of isobutene dimerization catalyzed by a macroporous sulphonic acid resin. *Appl. Catal. A, Gen.* **106**, 155–165 (1993).

32. Kamath, R. S., Qi, Z., Sundmacher, K., Aghalayam, P., & Mahajani, S. M. Process analysis for dimerization of isobutene by reactive distillation. *Ind. Eng. Chem. Res.* **45**, 1575–1582 (2006).

33. Song, X. & Sayari A. Sulfated zirconia-based strong solid-acid catalysts: recent progress. *Cat. Rev*. **38**, 329-412 (1996).

34. Himmel, D., Goll, S.K., Leito, I., & Krossing, I., A unified pH scale for all phases, *Angew. Chem. Int. Ed.* **49**, 6885-6888, (2010).

35. Viggiano, A. A., Henchman, M. J., Dale, F., Deakyne, C. A., & Paulson, J. F. Gas-phase reactions of weak Brønsted bases I^-, PO_3^-, HSO_4^-, FSO_3^-, and $CF_3SO_3^-$ with strong Brønsted acids H_2SO_4, FSO_3H, and CF_3SO_3H, A quantitative intrinsic superacidity scale for the sulfonic acids XSO_3H (X= HO, F, and CF_3). *J. Am. Chem. Soc*. **114**, 4299-4306, (1992).

Acknowledgements

This work, including synthesis, characterization and crystal structure analysis was funded by BASF SE (Ludwigshafen, Germany) and the U.S. Department of Defense, Defense Threat Reduction Agency (HDTRA 1-12-1-0053). Work performed at the Advanced Light Source is

supported by the Director, Office of Science, Office of Basic Energy Sciences, of the U.S. Department of Energy under Contract No. DE-AC02-05CH11231. A portion of this research used resources at the Spallation Neutron Source, a DOE Office of Science User Facility operated by the Oak Ridge National Laboratory. NMR work was supported as part of the Center for Gas Separations Relevant to Clean Energy Technologies, an Energy Frontier Research Center funded by the U.S. Department of Energy, Office of Science, Basic Energy Sciences under Award # DE-SC0001015. T.O.P. acknowledges funding from the NSF Graduate Research Fellowship Program. C.Y. acknowledges support from a Hewlett-Packard Stanford Graduate Fellowship. P.U. acknowledges the German Research Foundation (DFG, PU 286/1-1). M.J.K is grateful for financial support through the German Research Foundation (DFG, KA 4484/1-1). We acknowledge Bunyarat Rungtaweevoranit for his assistance with electron microscopy; Simon Teat and Laura McCormick for the synchrotron X-ray diffraction data acquisition support at beamline 11.3.1 of the Advanced Light Source, Lawrence Berkeley National Laboratory.

Author Contributions

C.T. and T.O.P co-wrote the manuscript. C.T. performed the PND modeling, SXRD and PXRD experiments. T.O.P. performed the solid state NMR experiments and NMR DFT calculations, with support and advice from J.R. J.S., Q.L. and J.B. performed the dimerization catalysis experiments with the support and advice of G.S. C.Y. performed the IR experiments. J.W. performed the DFT calculations on the cluster models, with support and advice from M.H.G. A.H. performed the PND experiments. P.U. performed the PXRD Rietveld refinements. M.K. helped with TGA experiments. J.J. supported and advised the synthesis. O.Y. supervised the project. All authors reviewed and edited the manuscript and contributed useful discussions.

Competing interests

The authors declare no competing interests.

Additional information

Supplementary information is available in the online version of the paper. Reprints and permissions information is available online at www.nature.com/reprints.

Correspondence and requests for materials should be addressed to O.Y.

Figure Captions

Fig. 1. **MOF-808, MOF-808-SO_4, and visualization of differences in molecular 'decoration.'** **(a)** Pristine MOF-808 is comprised of 6-connected zirconium-based metal clusters containing five formate groups and linked by benzenetricarboxylate (BTC) into the depicted spn topology framework. These formates may be substituted with sulfate anions as in **(b)**, which coordinate in a bidentate fashion to zirconium, either in chelating mode to a single zirconium atom, or in a bridging mode to two zirconium atoms. Sulfate is predominantly in the bridging mode in the solvated MOF, and converts exclusively to the chelating mode following activation by heating under dynamic vacuum. **(c)** Two representations of modeled zirconium clusters, with BTC-linkers omitted beyond the coordinating carboxylate group, highlight the differences in

molecular 'decoration' between clusters in the overall structure. A similar stoichiometry of hydroxide, water and sulfate groups are present on each cluster, but the local arrangement and apportionment of these groups differs between each cluster.

Fig. 2. Structural characterization of MOF-808-SO_4 by Rietveld refinement of powder neutron data, and NMR evidence for presence of water being central to the strong acid site. **(a)** The data obtained from powder neutron diffraction (red) is compared against the calculated pattern from the structural model (black), and their difference (blue). wRp = 2.91%, Rp = 9.59%. **(b)** ^{31}P MAS solid state NMR spectra of trimethylphosphine oxide (TMPO) adsorbed into (i) MOF-808-SO_4 (blue) and (ii) dehydrated MOF-808-SO_4 (red). The peak at 69 ppm, assigned to TMPO interacting with the strong Brønsted acid site, is lost upon dehydration. The peak centered at 42 ppm is due to excess TMPO that is not interacting with acid sites directly. Other peaks in the spectra belong to TMPO adsorbed at various μ^1-OH, μ^3-OH, and terminal water sites.

Fig. 3. Depiction of the zirconium cluster and Brønsted acid site in MOF-808-SO_4 as determined by DFT geometry optimization. (a) the overall cluster, **(b)** a close-up view of the acid site with relevant bond lengths and angles, with the acidic proton participating in the hydrogen bond labeled as H_a, and the other as H_b. Atoms not directly part of the active site are in grey, with zirconium in blue, oxygen in red, sulfur in yellow and hydrogen in white.

Fig. 4. Identification of the resonances attributable to adsorbed water using ^{1}H solid state NMR, comparing MOF-808-SO_4 before and after dehydration. (a) ^{1}H MAS spectrum of MOF-808-SO_4 at 6 kHz MAS (blue), ^{1}H MAS spectrum of dehydrated MOF-808-SO_4 at 6 kHz MAS (red), and their difference (black) showing the loss of two prominent peaks assigned as the two inequivalent protons on a water molecule hydrogen-bonded to sulfate. **(b)** ^{1}H DQ-MAS NMR spectrum of MOF-808-SO_4 with SQ and DQ skyline projections (blue). The spectrum was recorded at 12.5 kHz with two cycles of the BABA recoupling sequence for excitation and reconversion of DQ coherence. The two peaks that are lost upon dehydration appear at 2.5 and 8.7 ppm and exhibit a DQ coherence at 11.2 ppm, and are assigned as the inequivalent protons on terminal water hydrogen bonded to chelating sulfate. The prominent peak along the autocorrelation diagonal at 5 ppm is assigned as terminal water elsewhere on the zirconium cluster, not adjacent to sulfate.

Fig. 5. Comparison of the catalytic conversion, selectivity, and long-term stability of MOF-808-SO_4 and dehydrated MOF-808-SO_4 against benchmark catalysts. (a) General reaction scheme for the dimerization of isobutene (2-methylprop-1-ene) to isooctene (2,4,4-trimethylpent-1-ene, 2,4,4-trimethylpent-2-ene). **(b)** Plot of the percent conversion of isobutene to isooctene for MOF-808-SO_4 (blue), dehydrated MOF-808-SO_4 (red), sulfated zirconia (green), Amberlyst (orange) and H-ZSM-5 (pink) from room temperature up to 200 °C. Amberlyst is the most active at low temperatures while MOF-808-SO_4 has a strong temperature dependence. Dehydrated MOF-808-SO_4 has significantly lower conversion efficiency, indicating that the presence of water adjacent to chelating sulfate is responsible for the majority of the activity. **(c)** Plot of the selectivity for dimer products over higher order oligomers. Both Amberlyst and H-ZSM-5 have poor selectivity, favoring higher order oligomers at all temperatures. MOF-808-SO_4, dehydrated MOF-808-SO_4, and sulfated zirconia have nearly 100% selectivity for dimer products up to 80 °C **(d)** Plot of the long-term catalytic performance of MOF-808-SO_4 for the dimerization of

isobutene at 80 °C (blue), 120 °C (violet) and 160 °C (dark red), against sulfated zirconia (green) at 80 °C. The conversion efficiency for MOF-808-SO_4 is maintained at 80 °C, but at higher temperatures the material loses activity with an increasing rate, likely due to desorption of terminal water from the clusters at these temperatures. Sulfated zirconia at 80 °C has approximately one third of the activity of MOF-808-SO_4 at 80 °C, but falls to about half this value by 240 hours, while MOF-808-SO_4 maintains its conversion level throughout this period.

Table of contents graphic:

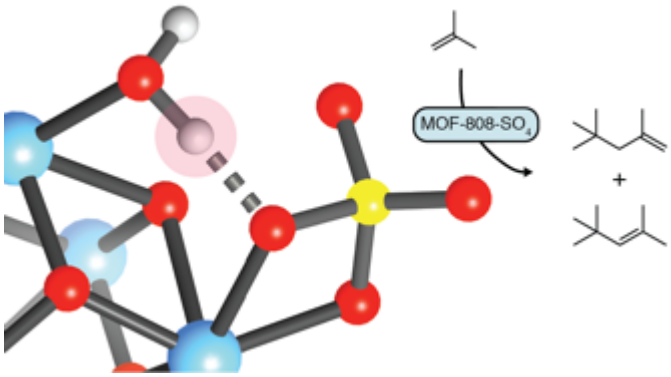

Figure 1:

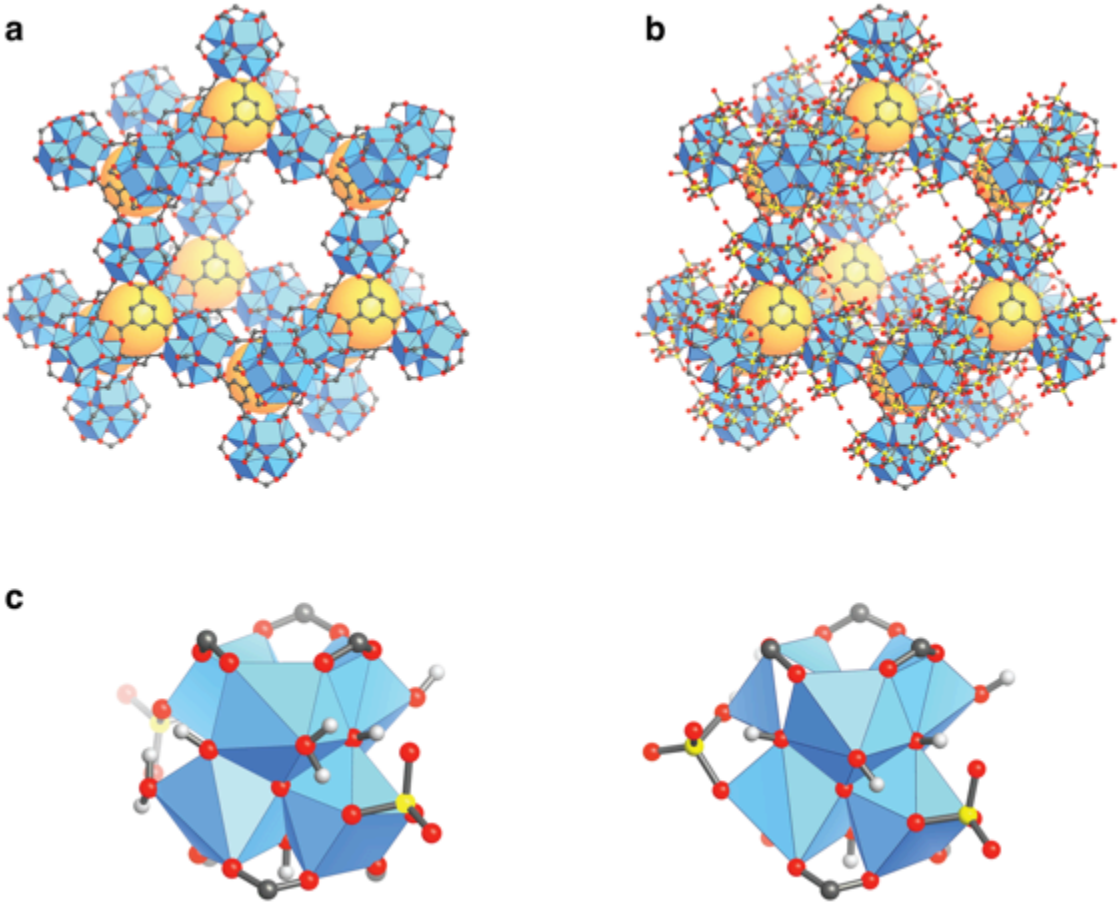

Figure 2:

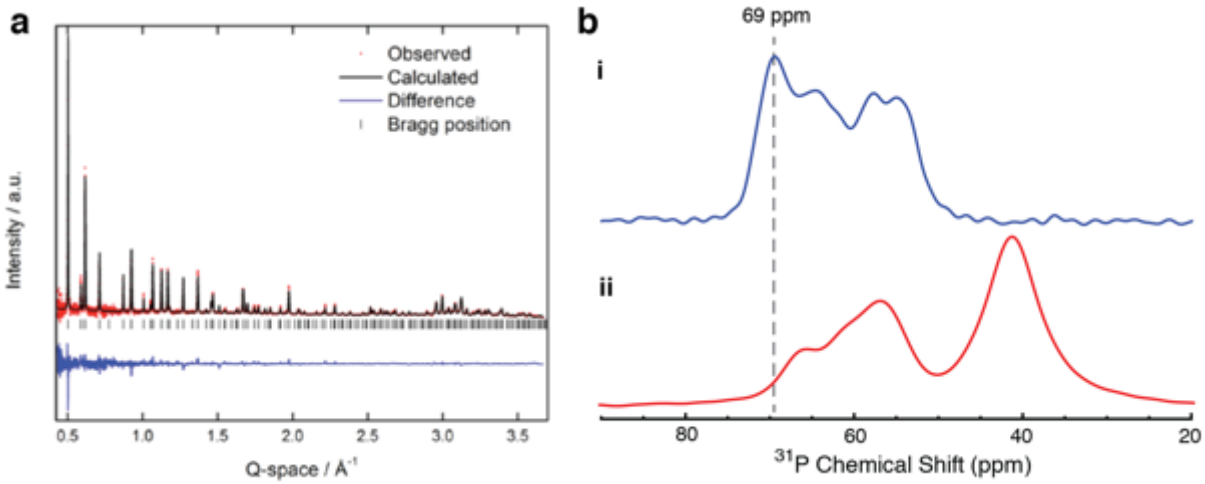

Figure 3:

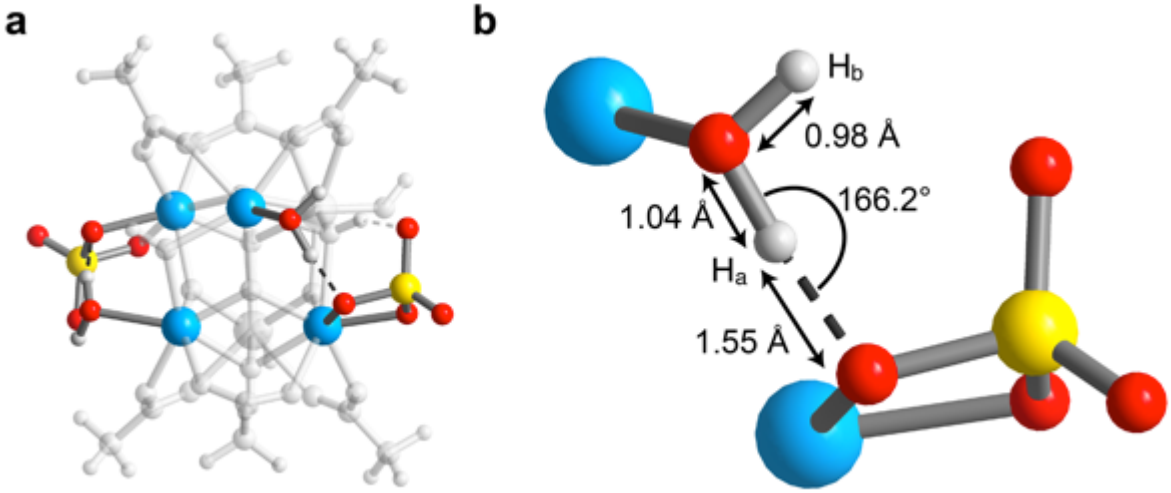

Figure 4:

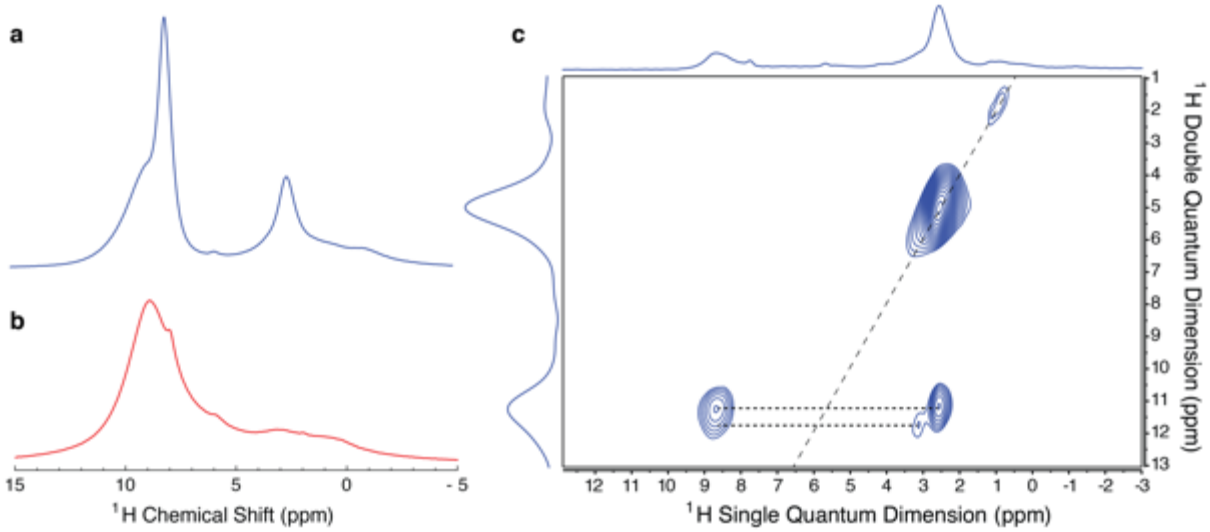

Figure 5:

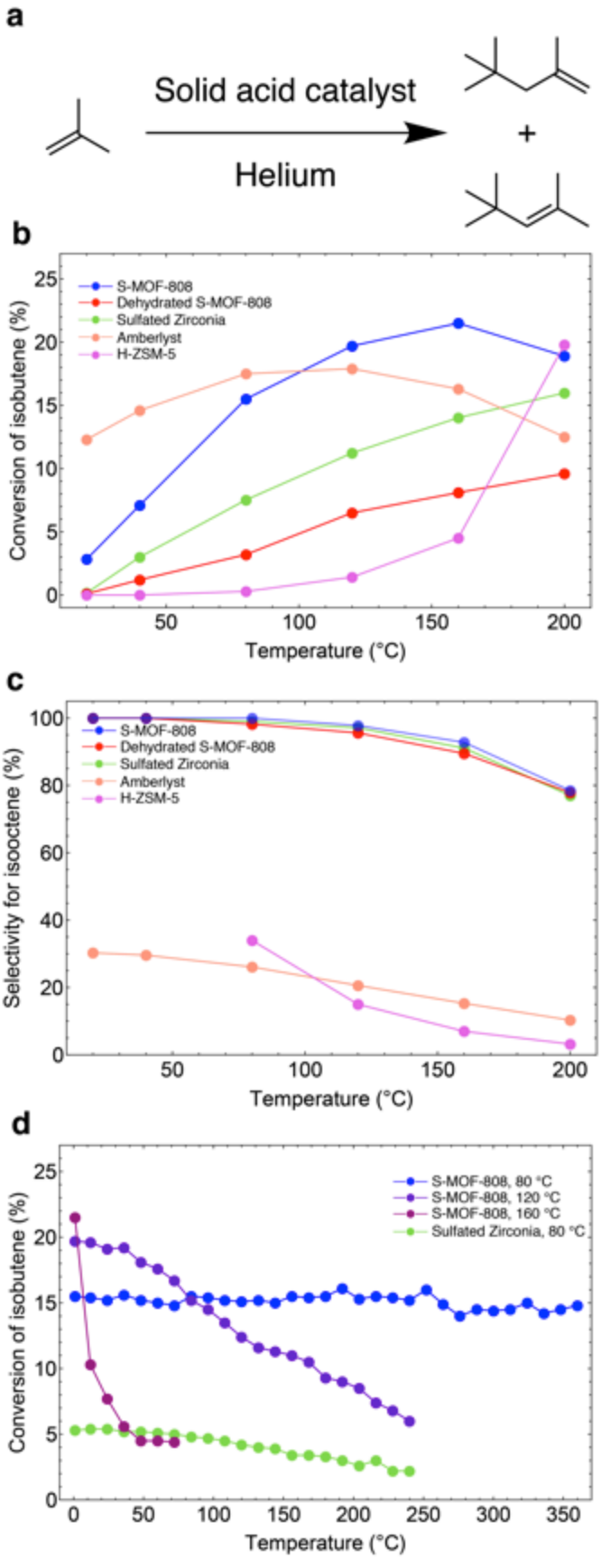
a
Solid acid catalyst
Helium
+
b
S-MOF-808
Dehydrated S-MOF-808
Sulfated Zirconia
Amberlyst
H-ZSM-5
Conversion of isobutene (%)
Temperature (°C)
c
Selectivity for isooctene (%)
Temperature (°C)
d
S-MOF-808, 80 °C
S-MOF-808, 120 °C
S-MOF-808, 160 °C
Sulfated Zirconia, 80 °C
Conversion of isobutene (%)
Temperature (°C)

Supplementary Information

Identification of the Strong Brønsted Acid Site in a Metal-Organic Framework Solid Acid Catalyst

Table of Contents

Section 1: Syntheses of Materials 2
Section 2: Powder Neutron Diffraction Experiments 4
Section 3: Single Crystal X-ray Diffraction Analyses 12
Section 4: Powder X-ray Diffraction Patterns, Rietveld 18
Section 5: Thermogravimetric Analysis 25
Section 6: N_2 Sorption Isotherms 28
Section 7: Solid State NMR Spectroscopy 31
Section 8: *In Situ* Infrared Spectroscopy 36
Section 9: Scanning Electron Microscopy 42
Section 10: Cluster Geometry Optimization 42
Section 11: Acid Catalysis of Isobutene 44
Section 12: References 44

Section 1: Syntheses of Materials

Methods.

Chemicals used in this work. *N,N*-dimethylformamide (DMF) was obtained from Fisher Scientific. Formic acid (purity > 98%) and anhydrous chloroform were obtained from EMD Millipore Chemicals. Anhydrous acetone was obtained from Acros Organics. Zirconium oxychloride octahydrate (>99.5%), hydrofluoric acid (aqueous, 48%), sulfuric acid (H_2SO_4, purity ≥ 95%), 1,3,5-benzenetricarboxylic acid (H_3BTC), selenic acid (aqueous, 40%) deuterated sulfuric acid (D_2SO_4, 96-98%, 99.5 atom % D) and D_2O (99.9 atom % D) was obtained from Aldrich. Deuterated 1,3,5-benzenetricarboxylic acid (D_3DBTC, 97%, 98 atom % D) was obtained from CDN Isotopes. Trimethylphosphine oxide (TMPO) was obtained from Alfa Aesar. Ammonium hydroxide (28%) was obtained from EMD Millipore. All starting materials and solvents, unless otherwise specified, were used without further purification.

Analytical techniques. Single-crystal x-ray diffraction (SXRD) data were collected on beamline 11.3.1 at the Advanced Light Source, Lawrence Berkeley National Lab. Samples were mounted on MiTeGen® kapton loops and placed in a 100(2) K nitrogen cold stream provided by an Oxford Cryostream 700 Plus low temperature apparatus on the goniometer head of a Bruker D8 diffractometer equipped with a PHOTON100 CMOS detector operating in shutterless mode. Diffraction data were collected using synchrotron radiation monochromated using a silicon (111) reflection to a wavelength of 0.7749(1) Å. An approximate full-sphere of data was collected using a combination of phi and omega scans with scan speeds of 2 seconds per 4 degrees for the phi fast scans, and 5 and 15 seconds per degree for the omega scans at 2θ = 0 and -45, respectively. In all cases, the data were processed using the Bruker APEX2 software package (*1*, *2*), structures were solved by intrinsic phasing (SHELXT) and refined by full-matrix least squares on F^2 (SHELXL-2014) using the Olex2 software package (*3*). All non-hydrogen atoms were refined anisotropically unless otherwise specified. Hydrogen atoms were geometrically calculated and refined as riding atoms. See Section 3 for more details.

Powder x-ray diffraction patterns (PXRD) were recorder using a Bruker D8 Advance diffractometer (Göbel-mirror monochromated Cu K_α radiation λ= 1.54056 Å). Elemental microanalyses (EA) for carbon, hydrogen, nitrogen and sulfur were performed in the Microanalytical Laboratory of the College of Chemistry at UC Berkeley, using a Perkin Elmer 2400 Series II CHNS elemental analyzer. Solution ^{1}H NMR spectra were acquired on a Bruker AVB-400 NMR spectrometer. N_2 sorption isotherms were measured on a Quantachrome Quadrasorb instrument, held at 77 K using a liquid nitrogen bath. Helium was used for the estimation of dead space for gas adsorption measurements. Ultra-high purity grade N_2 and He were used throughout the adsorption experiments.

Powder neutron diffraction data (PND) were collected at POWGEN at Oak Ridge National Laboratory, Tennessee. Two diffraction patterns were collected for each sample using center wavelengths 1.066 Å and 4.797 Å covering a d-spacing range of 0.5-15 Å.

Inductively coupled plasma-optical emission spectroscopy (ICP-OES) was performed on a PerkinElmer Optical Emission Spectrometer Optima 7000DV instrument. Scanning electron microscope (SEM) images were obtained using a Zeiss Gemini Ultra-55 analytical scanning electron microscope. FTIR spectra were collected in-house using a Bruker ALPHA Platinum ATR-FTIR Spectrometer equipped with a single reflection diamond ATR module.

General procedure for sample preparation. To reduce nucleation in the growth of MOF single-crystals, the inner surface of glass containers were rinsed with Sigmacote® siliconizing reagent, washed three times with acetone, and dried in oven before use. Following synthesis, the MOFs were washed with DMF. The molecular formulae of the MOFs were determined using a combination of elemental analysis (C, H, N and S), ^{1}H NMR (ratio of linker to formate) and ICP-OES (Zr, Se), and TGA-MS. A mixture of containing 20 μL of DMSO-*d6* and 580 μL of hydrofluoric acid (48 wt% in water) was used to digest 10 mg of each MOF for NMR measurements.

Native MOF-808 synthesis. Single crystals of MOF-808 was prepared following the reported procedure (*4*). Briefly, $ZrOCl_2 \cdot 8H_2O$ (0.032 g, 0.10 mmol) and H_3BTC (0.022 g, 0.10 mmol) were dissolved separately in 2 ml DMF, then both solutions were combined in a 20 ml scintillation vial and 4 ml formic acid was added. This mixture was then placed in a pre-heated oven at 100 °C for three days. Colorless block crystals were collected in 81% yield based on Zr. As-synthesized MOF-808 single crystals were immersed in anhydrous DMF for three days followed by water for three days, during which time the solvent was exchanged three times per day. The same conditions were used for the preparation of deuterated MOF-808, except deuterated D_3BTC was used as the starting reagent, and washing was performed in D_2O instead of H_2O.

Preparation of Sulfated MOF-808. Approximately 50 mg of MOF-808 was immersed in 0.05 M sulfuric acid in H_2O for 24 hours and stirred at regular intervals. The treated solid was then washed with H_2O, then solvent exchanged by immersion in anhydrous acetone before exchanging into chloroform. For each step, the samples were washed for three days with the solvent being decanted and freshly replenished three times per day. The chloroform in the solvent-exchanged crystals was removed under dynamic vacuum (30 mTorr) for 24 h at room temperature, followed by 8 h at 80 °C and a further 16 h at 120 °C. The same conditions were used for the preparation of deuterated sulfated MOF-808, except deuterated deuterated sulfuric acid in D_2O was used, and all aqueous washings were carried out with D_2O.

^{1}H solution NMR spectra of the digested, activated and sulfated MOF-808 (400 MHz, DMSO-*d6*): 8.61 (s, BTC), 8.10 (s, HCOOH), 7.92 (s, DMF), peak area ratio (BTC:HCOOH:DMF) = 6.0:0.05:0.3. Anal calcd for $Zr_6O_4(OH)_4(C_9H_3O_6)_2(SO_4)_{2.3}(OH)_{1.4}(OH_2)_{3.1}(C_3H_7NO)_{0.4}$ = $Zr_6O_{34.1}C_{19.2}H_{20.4}S_{2.3}N_{0.4}$: C = 16.2%; H, 1.4%; N, 0.4%; S, 5.2%. Found: C = 17.2%; H, 1.3%; N, 0.6%; S, 5.4%.

Preparation of Selenated MOF-808. Approximately 50 mg of MOF-808 was immersed in 0.05 M selenic acid in H_2O for 24 hours and stirred at regular intervals. The treated solid was then washed with H_2O, then solvent exchanged by immersion in anhydrous acetone before exchanging into chloroform. For each step, the samples were washed for three days with the solvent being decanted and freshly replenished three times per day. The chloroform in the solvent-exchanged crystals was removed under dynamic vacuum (30 mTorr) for 24 h at room temperature, followed by 8 h at 80 °C and a further 16 h at 120 °C.

^{1}H solution NMR spectra of the digested, activated and selenated MOF-808 (400 MHz, DMSO-*d6*): 8.64 (s, BTC), 7.85 (s, DMF), peak area ratio (BTC:HCOOH:DMF) = 6.00:0.00:0.5. Calculated formula $Zr_6O_4(OH)_4(C_9H_3O_6)_2(SeO_4)_{2.3}(OH)_{1.4}(C_3H_7NO)_{0.5}(H_2O)_{2.9}$ = $Zr_6O_{34}C_{19.5}H_{20.7}N_{0.5}Se_{2.3}$: C, 15.3%; H, 1.4%; N, 0.5%. Found: C, 15.4%; H, 0.9%; N, 0.7%.

Preparation of sulfated zirconia. The synthesis of sulfated zirconia was performed following a literature report of conventional sulfated zirconia with an additional step to prepare $Zr(OH)_4$ from $ZrOCl_2 \cdot 8H_2O$.(*5*) Briefly, 1g $ZrOCl_2 \cdot 8H_2O$ was placed in 10 mL NH_4OH (28%) and stirred overnight at room temperature. The slurry was filtered and washed in deionized water before being dried at 50 °C. 1g of the product, $Zr(OH)_4$, was stirred for 2 h in 10 mL aqueous H_2SO_4 (0.05 M). The solid product was subsequently filtered and dried at 100 °C for 24 h, followed by calcination at 550 °C for 2 h. The sulfur loading was found to be 3.45%.

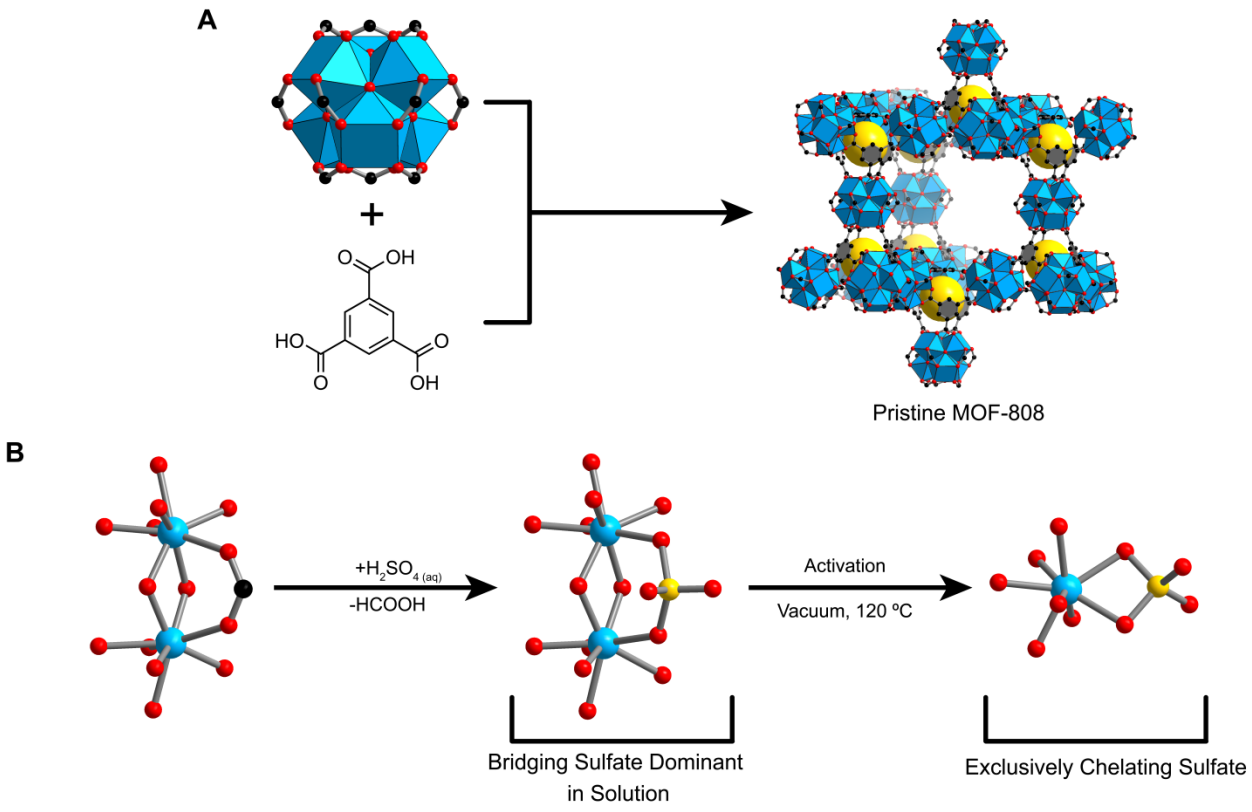

Supplementary Figure 1. Synthesis and coordination mode of sulfate in MOF-808-SO_4. **(A)** The synthesis of pristine MOF-808 constructed by 6-coordinate zirconium-based metal clusters containg formate groups and linked by benzenetricarboxylate into the diamond topology is depicted. Note that only five out of a possible six formates coordinate to the cluster, with water ligands replacing the last formate. These formates may be substituted with sulfate anions as in **(B)**, which coordinate in a bidentate fashion to zirconium, predominantly by a bridging mode to two zirconium atoms when in solution, and convert to exclusively the chelating mode to a single zirconium atom following activation by heating under dynamic vacuum.

Section 2: Powder Neutron Diffraction Experiments

Approximately 300 mg activated pristine deuterated MOF-808 was packed into a 6 mm vanadium can sealed with a titanium collar, copper gasket and aluminum lid in an argon glove box. After post-synthetic exchange with 0.05 M D_2SO_4 in D_2O followed by activation described in Section 1, sulfated deuterated MOF-808 was similarly loaded into the vanadium can. In both cases, data was collected at 10 K and 300 K for comparison.

Structure models were initially developed in Materials Studio 7.0 using the models from single crystal x-ray diffraction experiments as a starting point. These models were then refined against the powder neutron data, with atomic coordinates of the cluster and linker allowed to refine freely, with occupancies fixed based on the activated pristine MOF-808 model and knowledge of sulfate coordinates from the MOF-808-SO_4 sample prior to activation from single crystal and powder x-ray data.

Pristine MOF-808 modeling

An initial structural model was developed based on MOF-808 single crystal data collected prior to activation. All hydrogen atoms in the structure were converted to deuterium atoms except for hydrogen

on formate, which was not deuterated. To begin with, atomic coordinates were allowed to refine freely before being fixed at their converged values. With the linker and zirconium occupancies fixed at 100%, the thermal ellipsoids and occupancies of the remaining atoms were systematically refined. Note that the ellipsoids on the linker C1, C2, C3, and the ellipsoids of the μ_3-O and –OH pairs were constrained to be identical in order to aid refinement. The occupancies of the μ_3-O and –OH groups O2, O3, O4 and O5 refined to 47.9 ±1.0, 48.7 ±1.0, 50.7 ±3.2% and 49.5 ±3.2% respectively, meaning there has been no deprotonation of the μ_3-OH groups to account for charge-balancing. Note however that the data set collected at room temperature failed to converge O5, and allowing the position of O4 to refine freely moved it to intermediate coordinates between O4 and O5 in the data set collected at 10 K. This is not an indication that O5 is not present as it is observed in the 10 K data set, but simply an averaging of the two positions due to thermal motion.

The ellipsoids of D3A and D5, corresponding to μ_3-OD, failed to converge indicating only partial exchange of hydrogen with deuterium. If hydrogen is partially present, this does not reflect the true occupancy of deuterium at this position as ^{1}H and ^{2}D signals cancel each other out. This could be additionally compounded from the terminal position of the deuterium atoms that increase disorder and thermal motion as is observed for H4 on formate. The formate carbon and hydrogen atoms, C4 and H4, refine to 84.1 ±1.1% and 85.5 ±2.3%, fixed to 83.3% as consistent with NMR data. Refinement of O6, which accommodated oxygen from formate and terminal water molecules coordinated zirconium, converged at 97.9 ±0.8%, which is consistent with terminal hydroxide groups completing the charge-balancing of the framework, and hence not being removed following activation as was found in MOF-808-SO_4. The final refinement converged to wR_p = 3.20% and R_p = 11.20%.

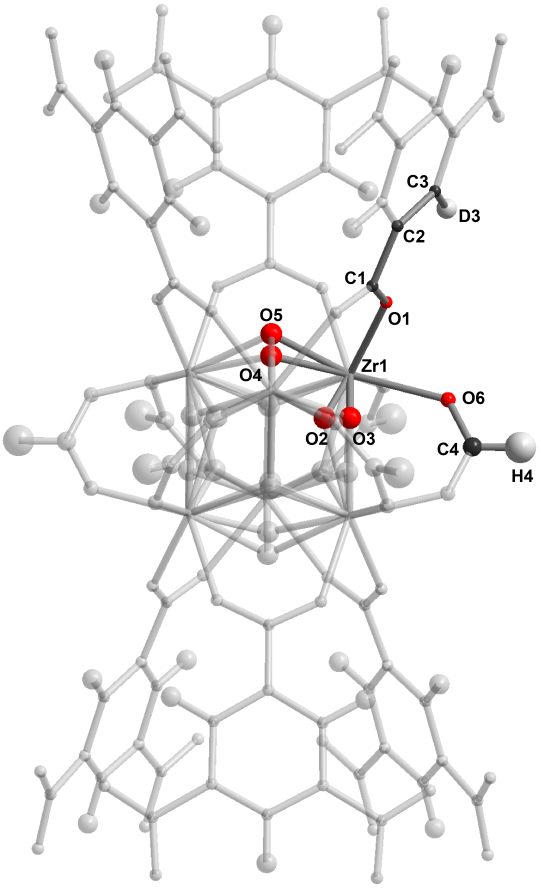

Supplementary Figure 2. Representation of metal oxide cluster in pristine MOF-808 as found by powder neutron diffraction. The asymmetric unit is colored and labeled with zirconium in blue, oxygen in red, carbon in black and hydrogen/deuterium in white, while the remaining atoms are shaded in order to show how the framework extends. Thermal ellipsoids are represented at 50% probability, with all refined isotropically. wRp = 3.20%, Rp = 11.20%

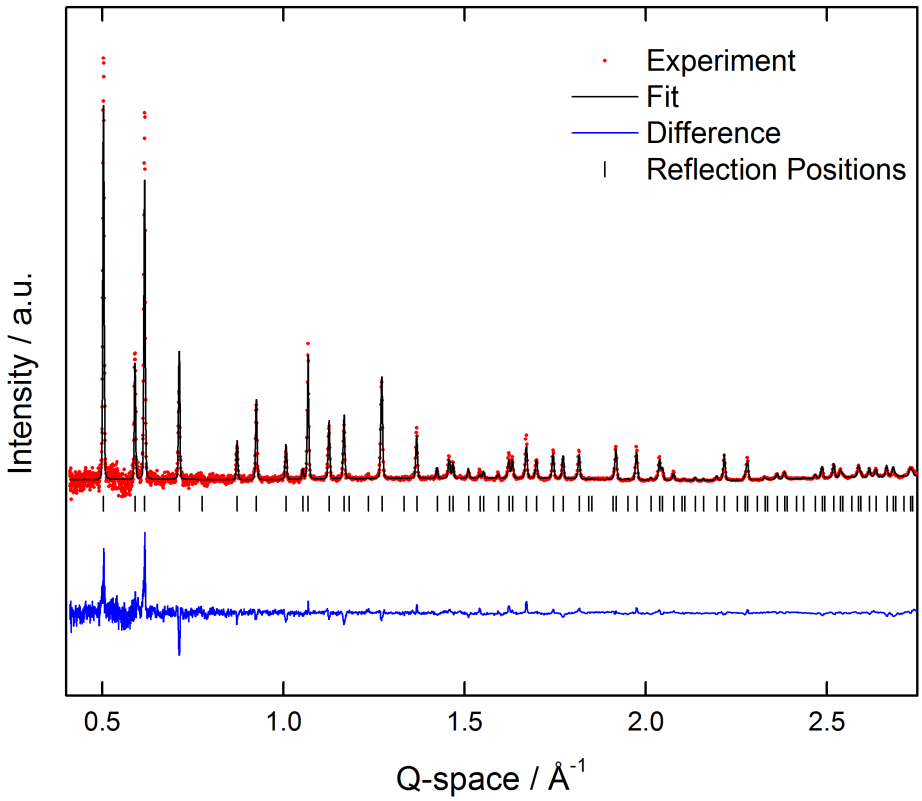

Supplementary Figure 3. Powder neutron diffraction pattern of data for pristine MOF-808 activated at 120 °C, displaying the experimental pattern (red) and the fitted pattern obtained by Rietveld refinement of the structure (black). The difference plot (blue) as well as the Bragg positions (black) are provided.

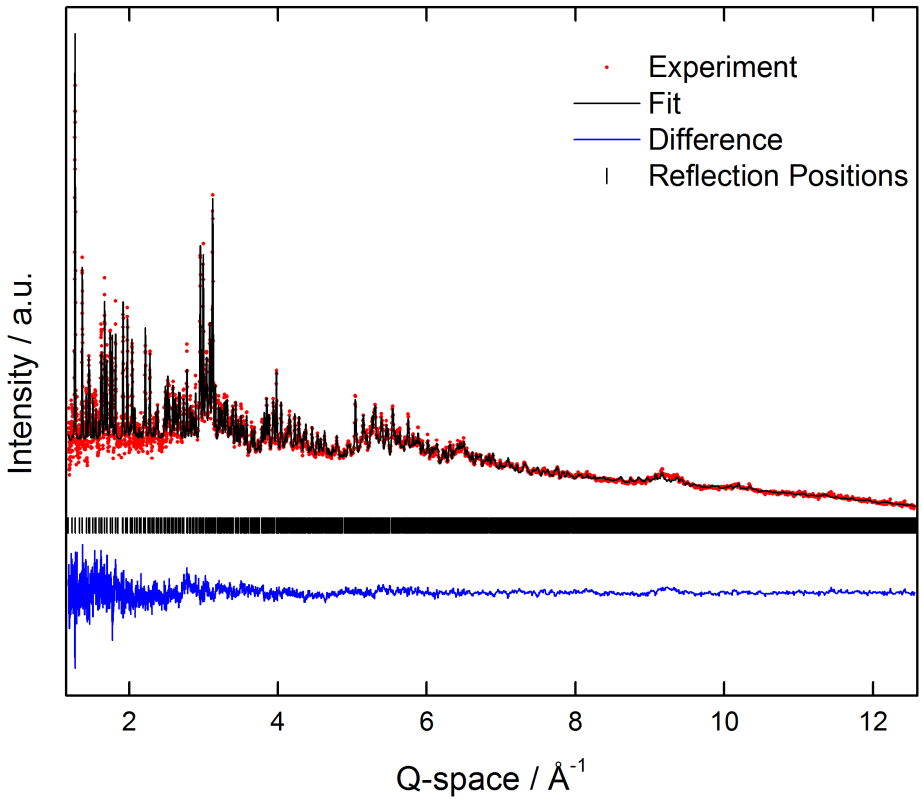

Supplementary Figure 4. Powder neutron diffraction pattern of data collected at high Q-space values for pristine MOF-808 activated at 120 °C, displaying the experimental pattern (red) and the fitted pattern obtained by Rietveld refinement of the structure (black). The difference plot (blue) as well as the Bragg positions (black) are provided.

MOF-808-SO_4 modeling

The coordinates and occupancies from the sulfated MOF-808 model prior to activation were imported and used as a starting point for Rietveld refinement. To begin with, atomic coordinates were allowed to refine freely before being fixed at their converged values. With the linker and zirconium occupancies fixed at 100%, the thermal ellipsoids and occupancies of the remaining atoms were systematically refined. Note that the ellipsoids on the linker C1, C2, C3, and the ellipsoids of the μ_3-O and –OH pairs were constrained to be identical in order to aid refinement. It was found that modeling S1, S2, O8A, O8B, O9A and O9B based on coordinates from single crystal data failed to converge with reasonable thermal ellipsoids. This is due to the very low occupancies of sulfate, found to be 12% and 6% for S1 and S2 in MOF-808-SO_4 respectively, and prior to activation. It should be noted that the coherent neutron scattering length for sulfur is less than half that of oxygen, in contrast with x-ray diffraction where sulfur contains double the number of electrons as oxygen and thus scatters x-rays much more readily. Since the refinement quality indicators, wR_p and R_p, displayed no significant difference between modeling and neglecting the sulfate groups, and requiring significant restraints to model whilst worsening the overall refinement quality, all sulfate atoms except for O6, which is oxygen bound to zirconium directly, were neglected in the final structure model. The presence of sulfate in the activated structure was however confirmed by elemental analysis and lack of formate by ^{1}H NMR, and evidence for the sulfate

position in the framework was identified through PXRD as being exclusively in the chelating mode (see Section 4).

Additionally, it was found that the thermal ellipsoid of D3A and D5, corresponding to deuterium on μ_3-OD in the framework, failed to converge. This could be evidence for deprotonated μ_3-OD in the framework; however, free refinement of the occupancies of the corresponding oxygen atoms on the μ_3-O and -OD groups, O2 (53.5 ±1.1%) and O3 (48.5 ±1.1%) for D3 and O4 (49.8 ±2.1%), O5 (50.8 ±2.1) for D5 were found to be, within two standard deviations, in an equal ratio as in the sample prior to activation. It is therefore presumed not all deuterium was successfully exchanged into the framework, since any hydrogen present in the same position has a negative scattering length and would negate the signal from deuterium. Indeed, a roughly 1:2 ratio of D to H would contribute overall no scattering. This could be additionally compounded from the terminal position of the deuterium atoms that increase disorder and thermal motion.

At position O6, where sulfate and water coordinate to zirconium in the sample prior to activation, the occupancy refines to 78.7 ±1.1%, yet the contribution from sulfate only accounts for 38.3%, or 4.6 oxygen atoms out of 12 possible sites per cluster. Since the remaining density must be derived from water, and having established charge-balancing is not achieved elsewhere, we postulate some of this density must be deprotonated water to become terminal hydroxide. Based on the chemical formula, there is an average charge of -1.4 per cluster unaccounted for, and therefore 11.7% of this density is assigned to hydroxide, or 1.4 out of the 12 possible positions per cluster, (two per zirconium). In total, sulfate and hydroxide account for 50% of the observed density, leaving 28.7 ±1.1% as water molecules bound to the zirconium cluster, which translates to 3.4 ±0.1 water molecules per cluster, and the remaining 21.6 ±1.1% unoccupied positions corresponding to open metal sites. This result is consistent with previous experimental data indicating Lewis acid sites alongside Brønsted acid sites in MOF-808-SO_4 (*4*). While the thermal ellipsoid for O6A is relatively large compared to other atoms in the structure, with at least three different species in different local environments and slightly different positions for each, this is reasonable. In the sample prior to activation with single crystal data, a larger anisotropic ellipsoid is also observed at position O6, reflecting the slightly strained conformation of the two binding modes of sulfate, which are not perfectly overlapping with the oxygen atom from coordinated water, which illustrates this point.

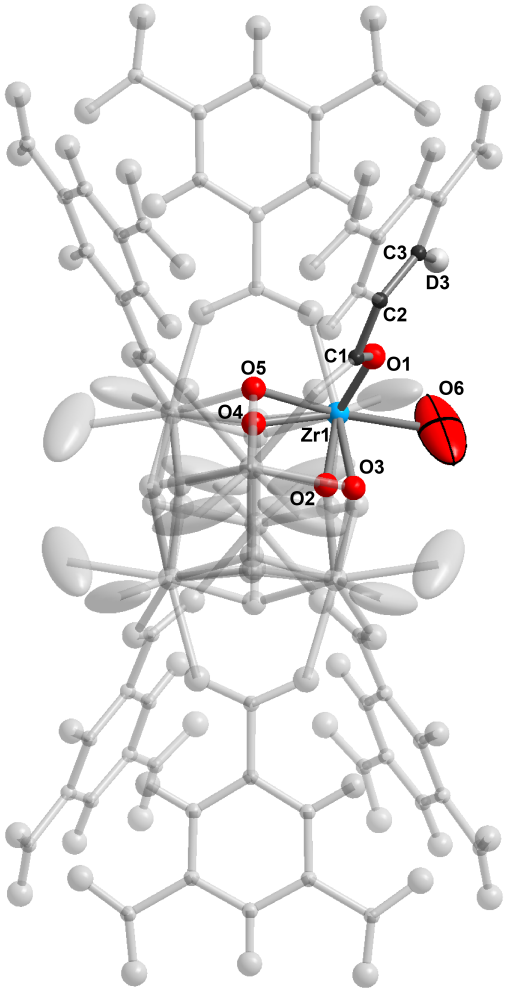

Supplementary Figure 5. Representation of metal oxide cluster in MOF-808-SO_4 as found by powder neutron diffraction. The asymmetric unit is colored and labeled with zirconium in blue, oxygen in red, carbon in black and deuterium in white, while the remaining atoms are shaded in order to show how the framework extends. Note the large ellipsoid for O6 relative to other atoms is expected as this position is representing at least four different sources of oxygen atoms including from water, hydroxide, bridging and chelating sulfate. Thermal ellipsoids are represented at 50% probability, with all except O6 refined isotropically. wRp = 2.91%, Rp = 9.59%

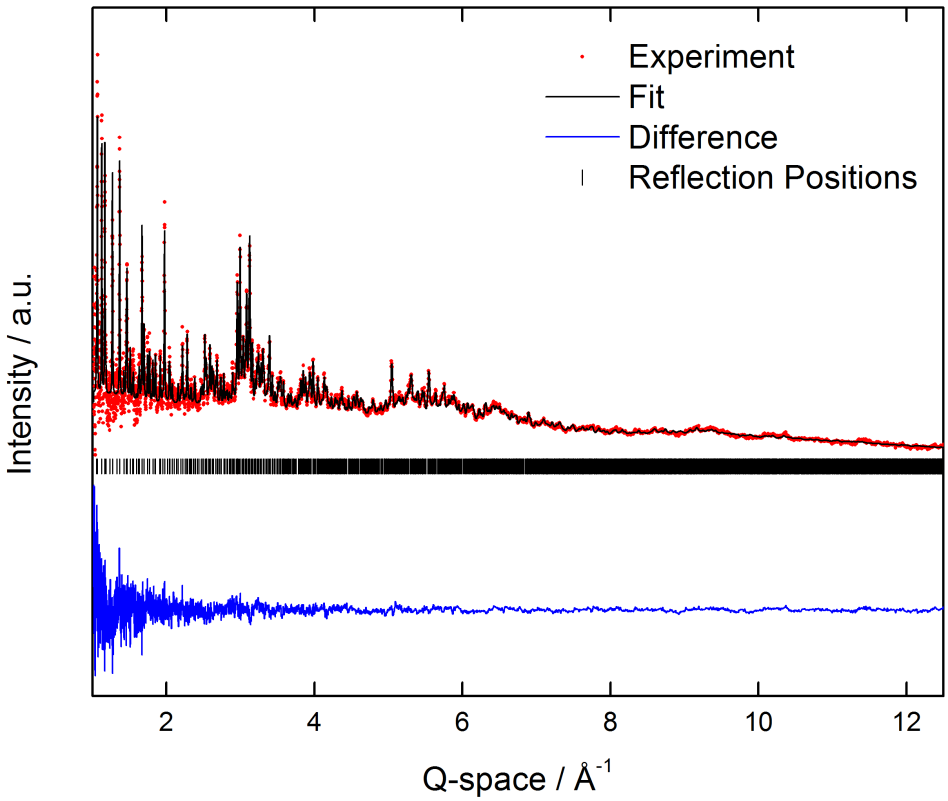

234

235 **Supplementary Figure 6.** Powder neutron diffraction pattern of data collected at high Q-space values for
236 MOF-808-SO_4 activated at 120 °C, displaying the experimental pattern (red) and the fitted pattern
237 obtained by Rietveld refinement of the structure (black). The difference plot (blue) as well as the Bragg
238 positions (black) are provided.

239

Section 3: Single Crystal X-ray Diffraction Analyses

Supplementary Table 1. Crystal structure data for pristine MOF-808 prior to activation.

Sample	**Pristine MOF-808**
chemical formula	$Zr_6O_{37.12}C_{23}H_{15}$
formula mass	1432.67
crystal system	cubic
space group	*Fd*-3*m*
λ (Å)	0.77490
a (Å)	35.1364(13)
Z	16
V (Å^3)	43378(5)
temperature (K)	100
size /mm	0.015 × 0.015 × 0.010
density (g/cm^{-3})	0.877
measured reflections	60241
unique reflections	2487
parameters	78
restraints	0
R_{int}	0.0858
θ range (deg)	2.10-30.74
R_1, wR_2	0.0531, 0.1907
S (GOF)	1.110
max/min res. dens. (e/Å^3)	0.75/-0.89

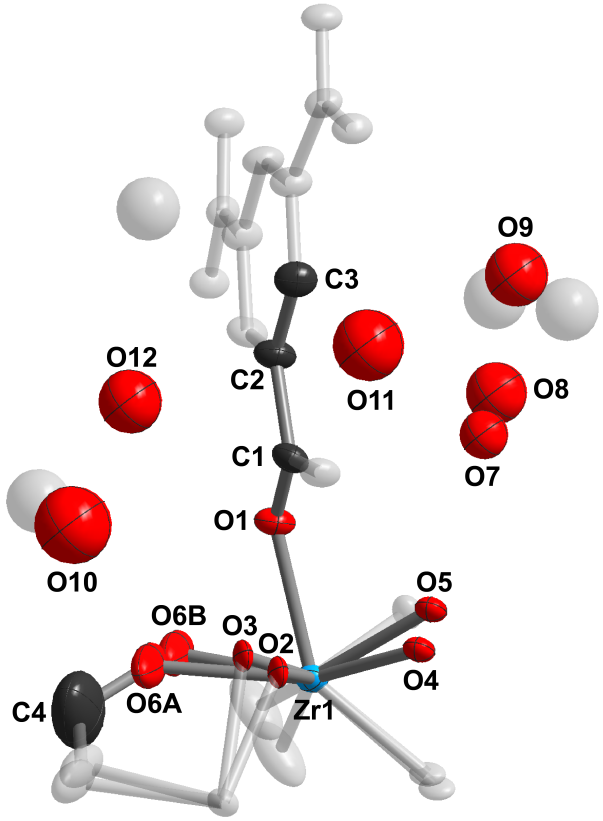

Supplementary Figure 7. Representation of pristine MOF-808 prior to activation from SXRD data. The asymmetric unit is displayed in color, with additional atoms in gray to aid visualizing the structure. Thermal ellipsoids are displayed at 50% probability and atom colors are as follows: zirconium (blue), oxygen (red), carbon (black), sulfur (yellow). Hydrogen atoms are omitted for clarity.

The single crystal structure of MOF-808-SO_4, while previously reported, was re-collected with the aim of carefully investigating the sulfate positions and their relative ratios. Thus, the occupancy of sulfur was permitted to refine freely, with S1 (bridging mode) refining to 12.0 ±0.3%, and S2 (chelating mode) to 5.8 ±0.7%. S1 is split by a mirror plane and thus the total sulfate occupancy relative to zirconium is 29.8 ±1.3%, and corresponds to a 4:1 ratio of bridging to chelating sulfate in the pre-activated form. Note this configuration changes to exclusively chelating upon activation under dynamic vacuum at 120 °C. Ellipsoids of O2 and O3, O4 and O5, O6A and O6B were constrained in their pairs to be identical due to their close proximity. Oxygen atoms have been modeled within the cavity of the structure, representing highly disordered solvent molecules which are typically hydrogen bonding to the framework and are likely a combination of water and DMF molecules. Note that O11 and O12 have been modeled isotropically due to their low occupancy and proximity to other atoms in the model. The geometry of sulfate was restrained to its known tetrahedral configuration using distance and angle restraints due to partial occupancy and positional overlap with solvent molecules.

Supplementary Table 2. Crystal structure data for MOF-808-SO_4 prior to activation.

Sample	MOF-808-SO_4
chemical formula	$Zr_6O_{43.09}C_{18}H_{10}S_{1.79}$
formula mass	1520.35
crystal system	cubic
space group	*Fd*-3*m*
λ (Å)	0.77490
a (Å)	35.2075(13)
Z	16
V (Å^3)	43642(5)
temperature (K)	100
size /mm	0.015 × 0.015 × 0.010
density (g/cm^{-3})	0.926
measured reflections	70715
unique reflections	3175
parameters	101
restraints	7
R_{int}	0.0849
θ range (deg)	2.09-33.75
R_1, wR_2	0.0556, 0.1911
S (GOF)	1.117
max/min res. dens. (e/Å^3)	1.1/-0.6

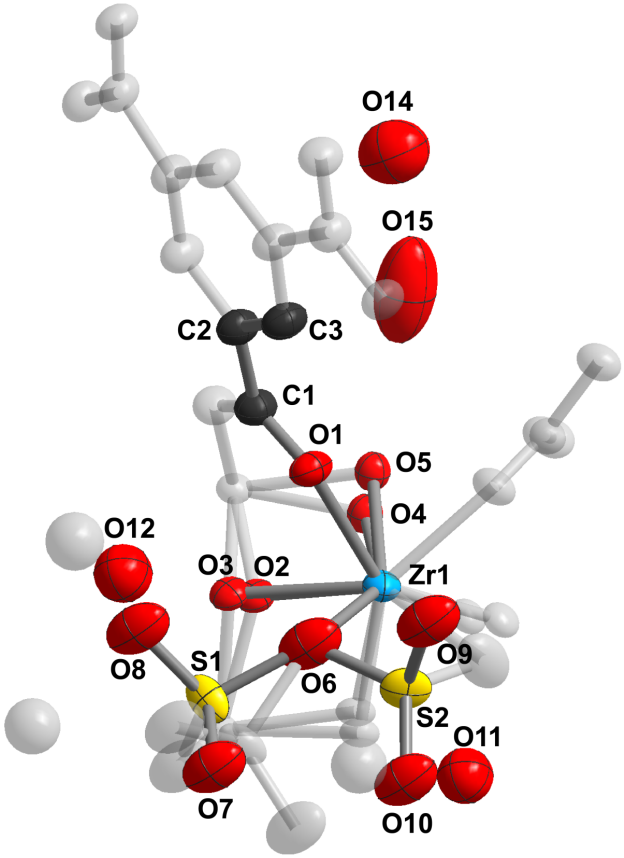

Supplementary Figure 8. Representation of MOF-808-SO_4 prior to activation from SXRD data. The asymmetric unit is displayed in color, with additional atoms in gray to aid visualizing the structure. Thermal ellipsoids are displayed at 50% probability and atom colors are as follows: zirconium (blue), oxygen (red), carbon (black), sulfur (yellow). Hydrogen atoms are omitted for clarity.

The single crystal structure of MOF-808-SeO_4 was modeled where the occupancy of sulfur was permitted to refine freely, with Se1 exclusively existing in the bridging mode in the pre-activated form. Note this configuration changes to exclusively chelating upon activation under dynamic vacuum at 120 °C. Ellipsoids of O2 and O3, O4 and O5, O6A and O6B were constrained in their pairs to be identical due to their close proximity. Oxygen atoms have been modeled within the cavity of the structure, representing highly disordered solvent molecules which are typically hydrogen bonding to the framework and are likely a combination of water and DMF molecules. Note that O7 through to O15 have been modeled isotropically due to their low occupancy and proximity to other atoms in the model. The geometry of selenate was restrained to its known tetrahedral configuration using distance and angle restraints due to partial occupancy and positional overlap with solvent molecules. Two low-angle reflections, (222) and (044), were omitted from the refinement due to their large discrepancy between calculated and experimental values. The reason for discrepancy is likely related to not fully accounting for the highly disordered solvent within the cavity.

Supplementary Table 3. Crystal structure data for MOF-808-SeO_4 prior to activation.

Sample	MOF-808-SeO_4
chemical formula	$Zr_6O_{43.90}C_{18}H_{10}Se_{1.28}$
formula mass	1579.22
crystal system	cubic
space group	*Fd*-3*m*
λ (Å)	0.77490
a (Å)	35.2645(10)
Z	16
V (Å^3)	43854(4)
temperature (K)	100
size /mm	0.015 × 0.015 × 0.010
density (g/cm^{-3})	0.955
measured reflections	79733
unique reflections	2245
parameters	98
restraints	17
R_{int}	0.0858
θ range (deg)	1.8-29.5
R_1, wR_2	0.0510, 0.1672
S (GOF)	1.144
max/min res. dens. (e/A^3)	0.8/-0.4

288

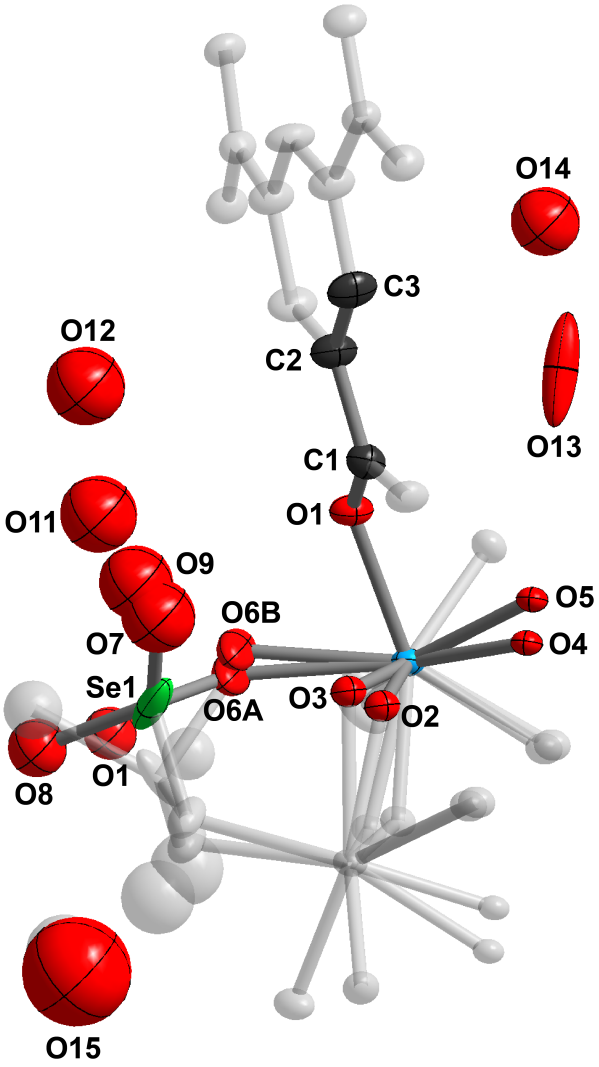

Supplementary Figure 9. Representation of MOF-808-SeO_4 prior to activation from SXRD data. The asymmetric unit is displayed in color, with additional atoms in gray to aid visualizing the structure. Thermal ellipsoids are displayed at 50% probability and atom colors are as follows: zirconium (blue), oxygen (red), carbon (black), selenium (green). Hydrogen atoms are omitted for clarity.

Section 4: Powder X-ray Diffraction Patterns, Rietveld

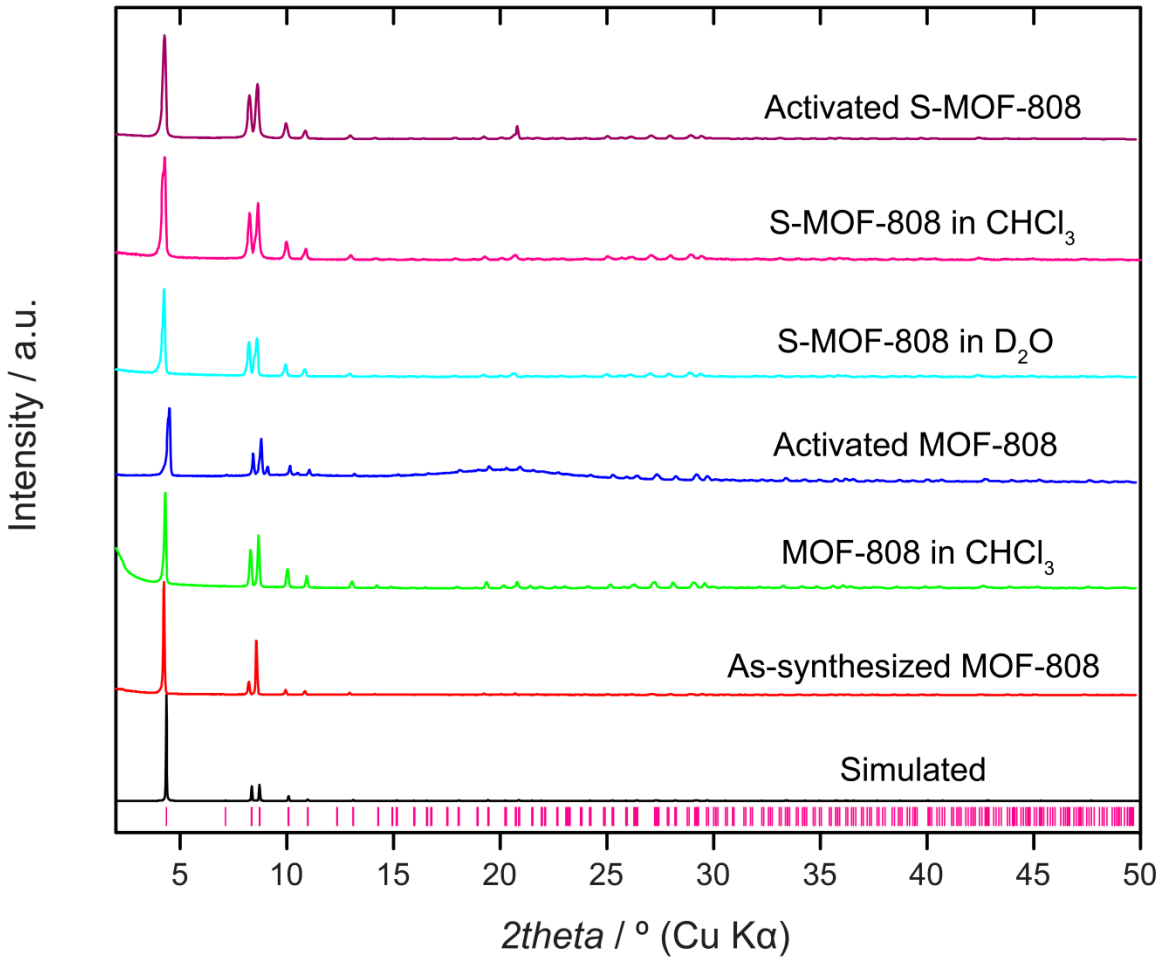

Supplementary Figure 10. PXRD patterns of deuterated MOF-808 after various stages of treatment. The pristine simulated pattern (black) is compared to the as-synthesized (red), after $CHCl_3$ (green), and after activation under dynamic vacuum (dark blue) of the pristine sample. The remaining patterns are immediately after treatment with D_2SO4 in D_2O (light blue), exchanging with $CHCl_3$ (pink) and activation of the sulfated sample (violet), showing crystallinity is retained.

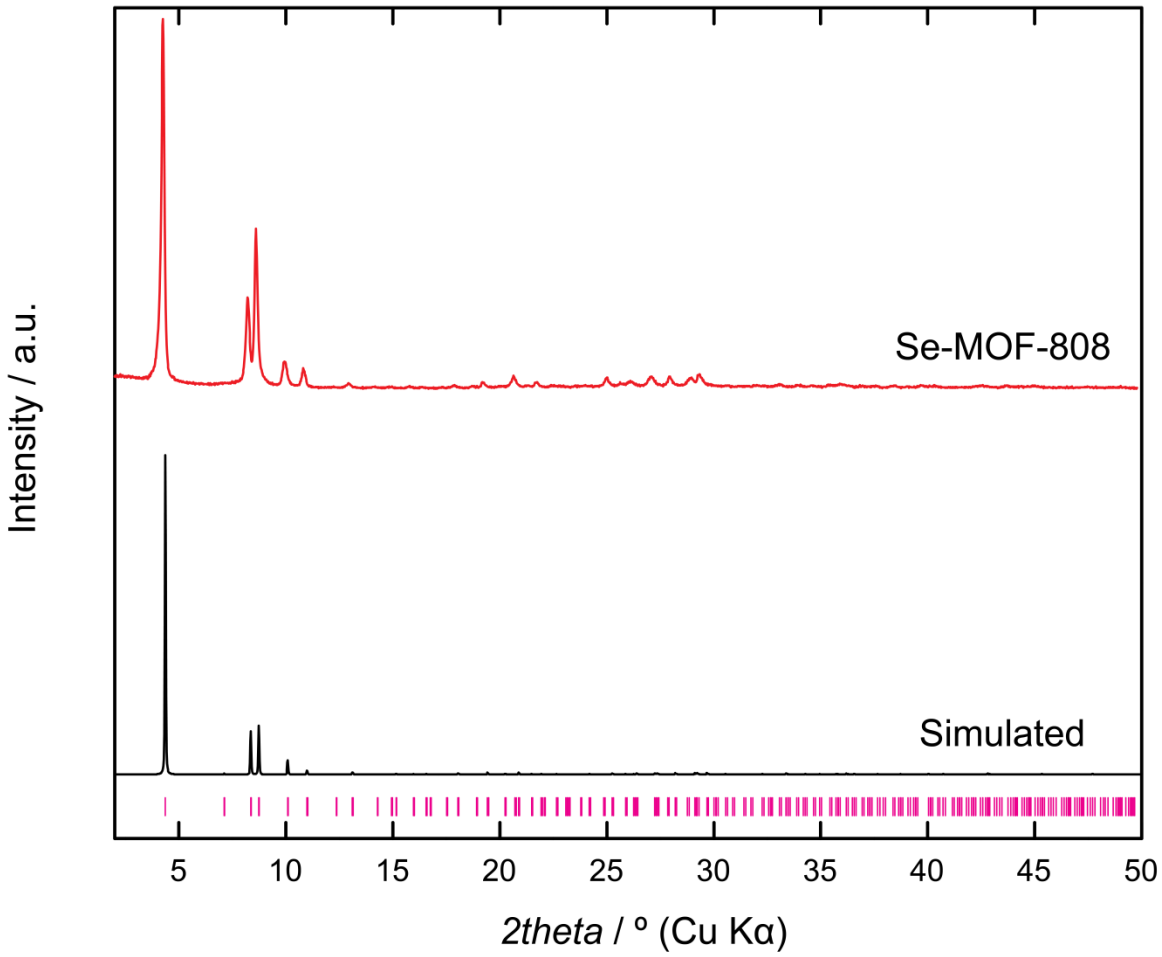

Supplementary Figure 11. PXRD patterns of simulated MOF-808 (black) and after immersion with 0.05 M of selenic acid, solvent exchange and activation (red).

X-ray powder Rietveld refinements of the activated samples under argon (both MOF-808-SeO_4 and MOF-808-SO_4) were carried out using TOPAS 5 (*6*). Regarding the overall quality of the fits, it is noted that there is no routine like Platon SQUEEZE used, which could take the contribution of any residual density in the pores into account, such as the disordered argon atoms or any other remaining molecules. Thus, there are small systematic deviations visible in the difference plots, which might be due to anything what is left in the pores. Also, reflections 111 and 022 had to be excluded from the refinements, as the inclusion of those two reflections rendered the refinement unstable and yielded chemically unreasonable electron densities in the F_{obs}-F_{calc} plots. This data was used to determine the position of selenate and sulfate only, and the neutron data collected from the spallation source was used for occupancies and thermal ellipsoid parameters discussed in the main text due to the superior data quality and resolution obtained.

In the first steps of the refinement, a structure model was used without selenate/sulfate groups. In subsequent steps, those groups were located after inspection of the F_{obs}-F_{calc} plots. Geometrical constraints were applied during the refinement to retain symmetry *Fd3̄m*: In

particular, the Zr_6-octahedra were allowed to expand/contract isotropically. The phenyl ring of the BTC linker was allowed to move along the 3-fold axis. The angle between the center of the phenyl ring, the carbon atom the carboxylate group is binding to and the carboxylate carbon, however, were refined freely, as a slight distortion of the linker was observed in previous work (*4*). Interatomic distances within the linker were constrained to their ideal values. Further constraints were applied to all oxygen atoms bound to the cluster and the selenate/sulfate as well as S/Se atoms themselves, to ensure they stayed on their ideal Wyckoff position. Anti-bump restraints were applied to the terminal oxygen atoms bound to S/Se. As of the low x-ray scattering contrast of hydrogen, no hydrogen atoms were refined other than the ones directly bound to the linker. In total, 3 isotropic displacement parameters were refined for the Se data. Specifically, one displacement parameter for the zirconium atom, one for all light elements besides the oxygens bridging zirconium and Se, and one for the selenate group. The results are as expected: $U_{iso}(Zr) < U_{iso}(\text{light atoms}) < U_{iso}(\text{selenate})$. The occupancy of the selenate/sulfate group was allowed to refine freely and is within the limits of the method and in reasonable agreement with the results from ICP and EA respectively. It has to be noted that the fit is worse for the S data than for Se. A reason for this could be the lower resolution. As a consequence, less parameters were refined. In particular the displacement parameters were fixed at reasonable values (0.03 for Zr, 0.05 for light atoms and 0.08 for the sulfate group). The chelating position of the sulfate group however was verified by inspecting the F_{obs}-F_{calc} plots. No significant electron density was found at a hypothetical bridging position.

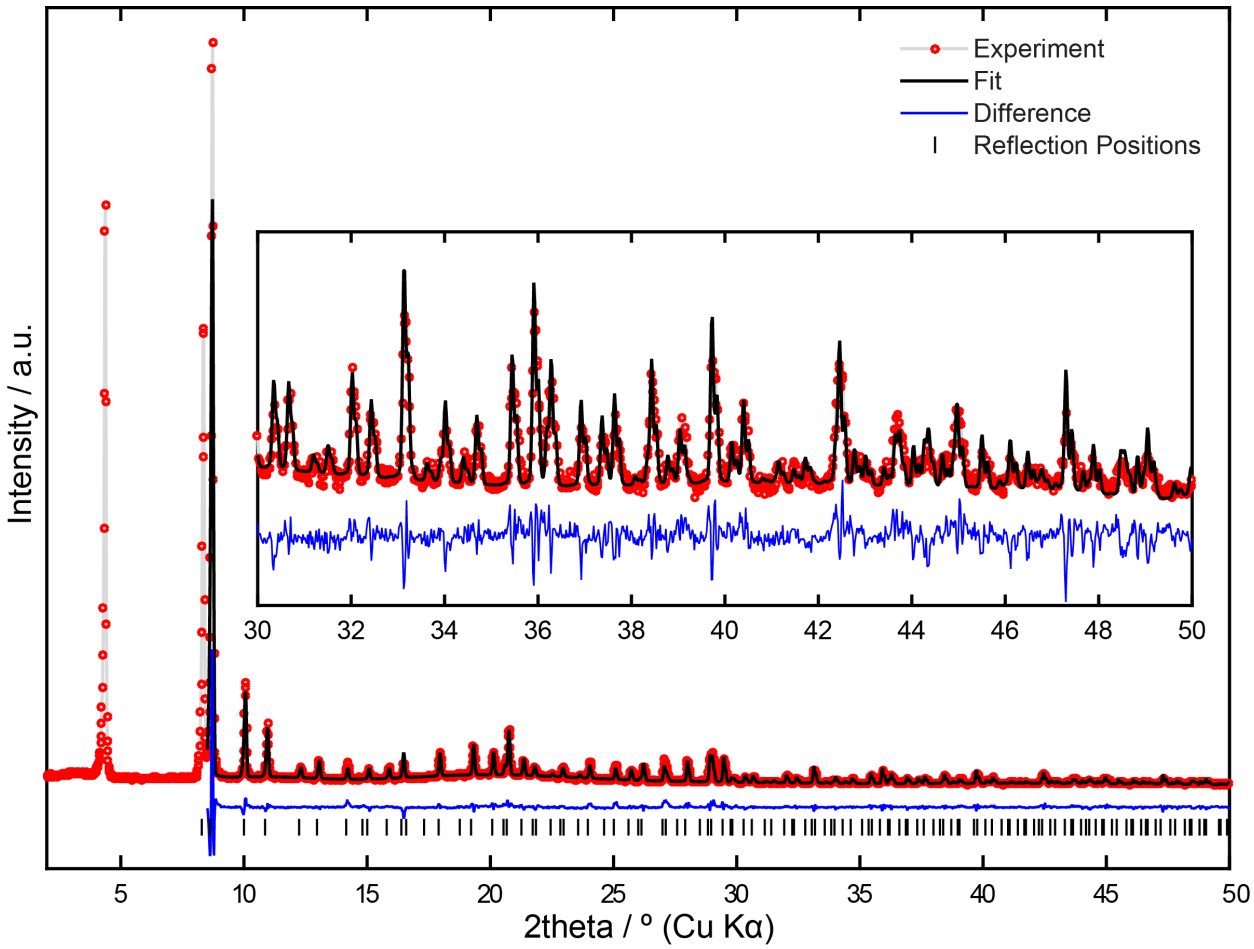

Supplementary Figure 12. Powder x-ray diffraction pattern of MOF-808-SO_4 activated at 120 °C, displaying the experimental pattern (red) and the fitted pattern obtained by Rietveld refinement of the structure (black). The difference plot (blue) as well as the Bragg positions (black) are provided. The data was collected under argon atmosphere at room temperature.

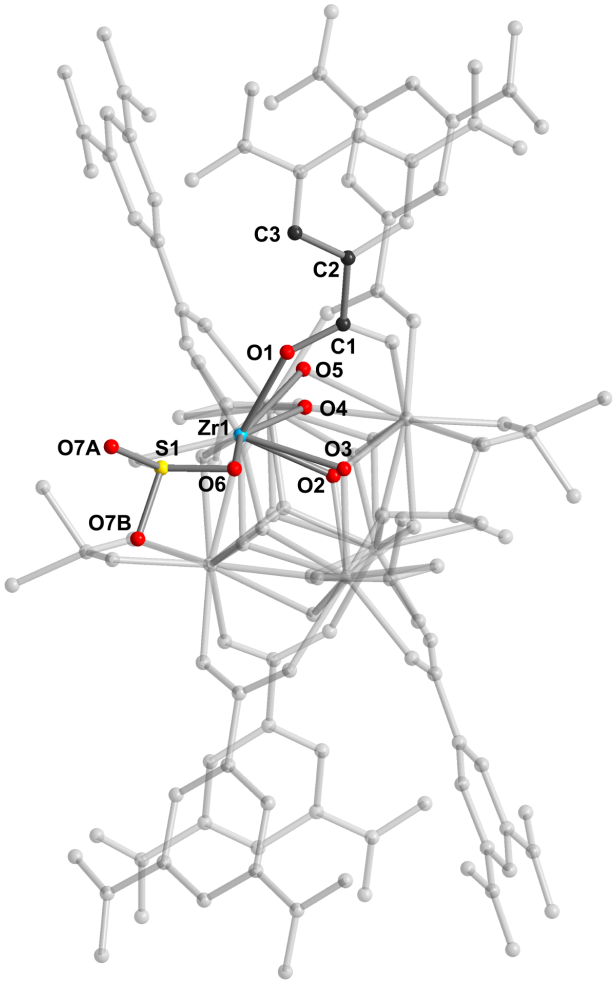

Supplementary Figure 1. Representation of metal oxide cluster in MOF-808-SO_4 as found by powder x-ray diffraction, revealing the exclusively chelating mode of sulfate. The asymmetric unit is colored and labeled with zirconium in blue, oxygen in red, carbon in black and sulfur in yellow, while the remaining atoms are shaded in order to show how the framework extends. Hydrogen atoms were omitted for clarity. Thermal ellipsoids are represented at 50% probability, with all refined isotropically. Rp = 11.6%.

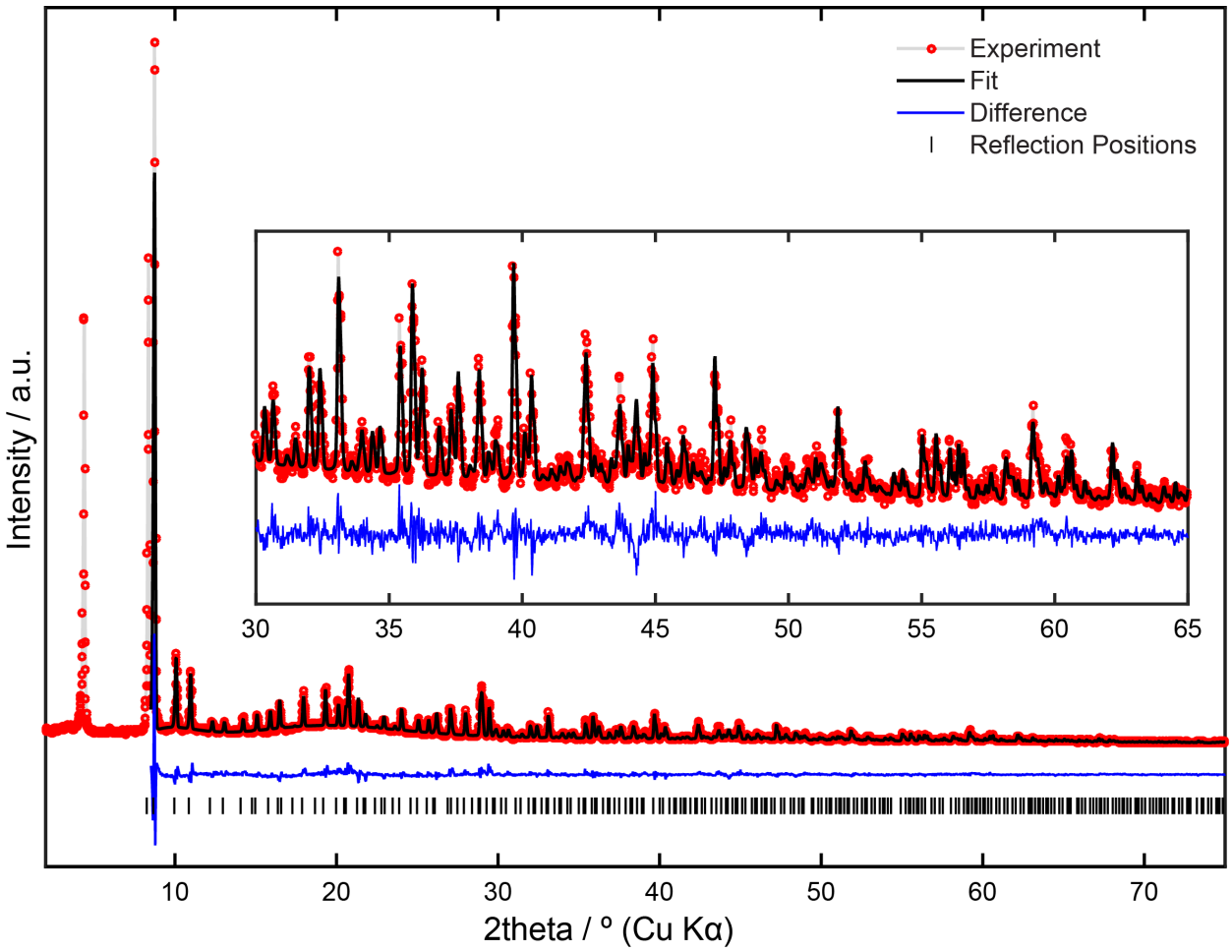

Supplementary Figure 2. Powder x-ray diffraction pattern of MOF-808-SeO_4 activated at 120 °C, displaying the experimental pattern (red) and the fitted pattern obtained by Rietveld refinement of the structure (black). The difference plot (blue) as well as the Bragg positions (black) are provided. The data was collected under argon atmosphere at room temperature.

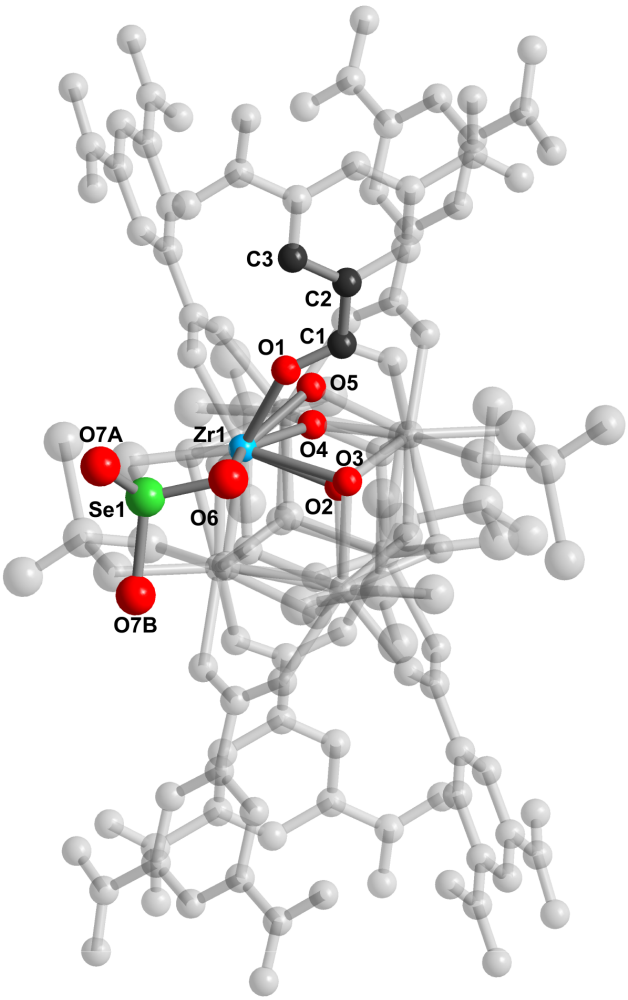

Supplementary Figure 3. Representation of metal oxide cluster in MOF-808-SeO_4 as found by powder x-ray diffraction, revealing the exclusively chelating mode of selenate. The asymmetric unit is colored and labeled with zirconium in blue, oxygen in red, carbon in black and sulfur in yellow, while the remaining atoms are shaded in order to show how the framework extends. Hydrogen atoms were omitted for clarity. Thermal ellipsoids are represented at 50% probability, with all refined isotropically. Rp = 10.5%.

Section 5: Thermogravimetric Analysis

Thermogravimetric analysis coupled to a mass spectrometer (TGA-MS) was performed using a Netzsch STA 449 F5 Jupiter thermogravimetric analyzer coupled to a Netzsch QMS 403 D Aeolos mass spectrometer. A typical sample preparation method is as follows: the activated MOF sample was weighed in a glove box under argon atmosphere and transferred under argon to the TGA-MS. The sample chamber was then evacuated three times, refilling the chamber each time with argon. Next, the sample was heated at a rate of 2 °C min^{-1} to 800 °C with an argon flow rate of 20 ml min^{-1}. The water signal was quantified by repeating the experiment under identical conditions but with copper sulfate pentahydrate as a standard since this compound has well-characterized water loss steps. The area underneath the water signal plot was then used to quantify the amount of water being lost in the MOF by relating this to the known amount lost in the standard. The first water signal, peaking at 143 °C, corresponds to 0.96 mg H_2O in 24.5 mg MOF-808-SO_4, which is 3.9% of the total mass. Taking the chemical formula of $Zr_6O_4(OH)_4(C_9H_3O_6)_2(SO_4)_{2.3}(OH)_{1.4}(OH_2)_x(DMF)_{0.4}$ = $Zr_6O_{31+x}C_{19.2}H_{14.2+2x}S_{2.3}N_{0.4}$, and assuming all terminal water molecules are lost after the first peak, then x = 3.1. This result is consistent with the PND data which indicates 3.4 ±0.1 water molecules per cluster. A similar calculation was performed on MOF-808-SeO_4, containing 3.4% H_2O by weight. Considering the formula $Zr_6O_4(OH)_4(C_9H_3O_6)_2(SeO_4)_{2.3}(OH)_{1.4}(C_3H_7NO)_{0.5}(H_2O)_x$ = $Zr_6O_{31.1}C_{19.5}H_{14.9}N_{0.5}Se_{2.3}$ + xH2O, then x = 2.9.

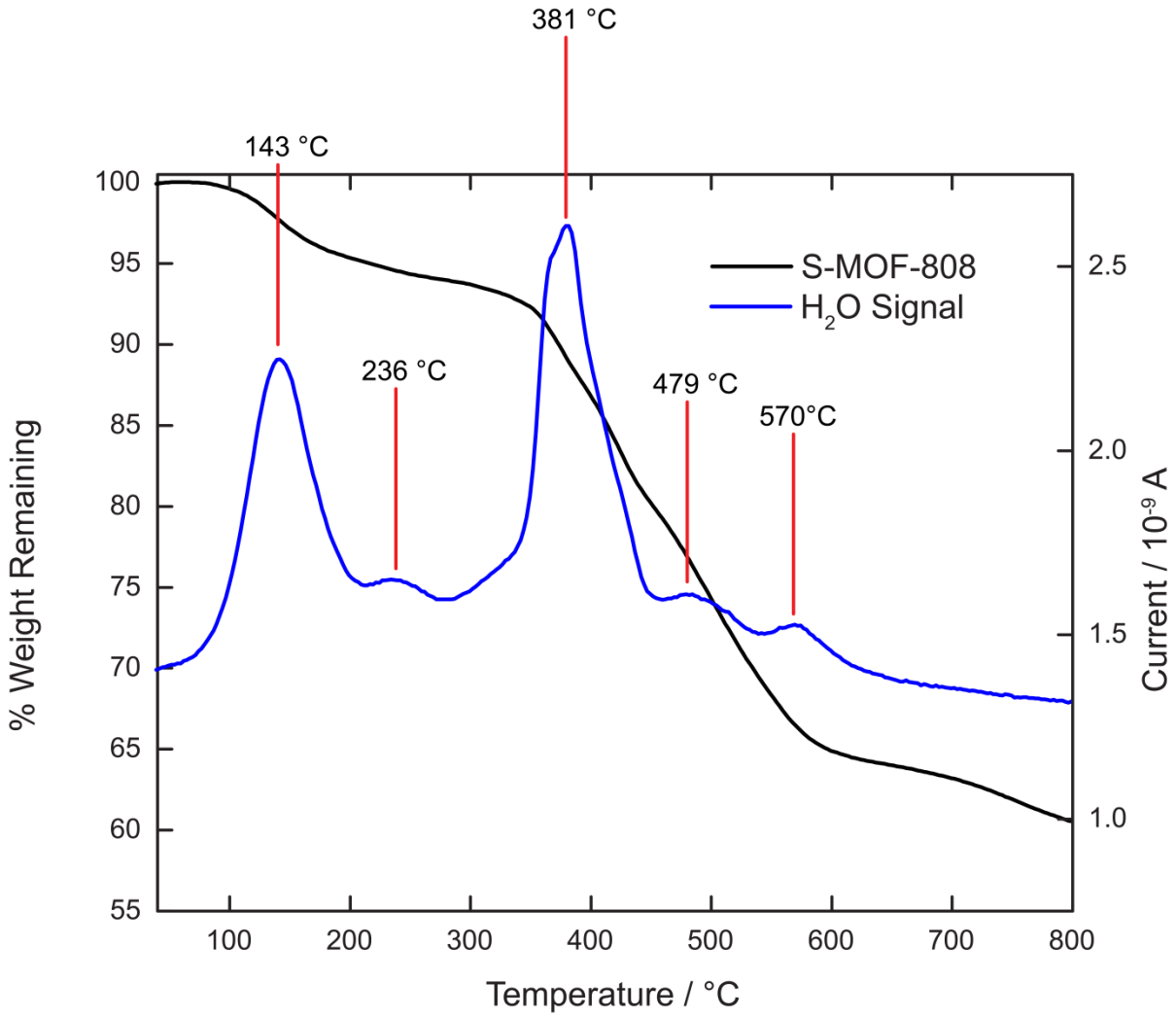

Supplementary Figure 4. TGA-MS plot of activated MOF-808-SO_4 under argon atmosphere with the thermogravimetric plot (black) and corresponding water loss signal (blue). The first mass loss, with the water signal peaking at 143 °C, corresponds of water coordinated to the framework that is lost prior to full structure decomposition beginning around 320 °C. Quantification of the water signals correspond to 3.1 water molecules per cluster for the first peak centered at 143 °C, 0.05 water molecules per cluster at 236 °C, and 4.5 water molecules at 381 °C.

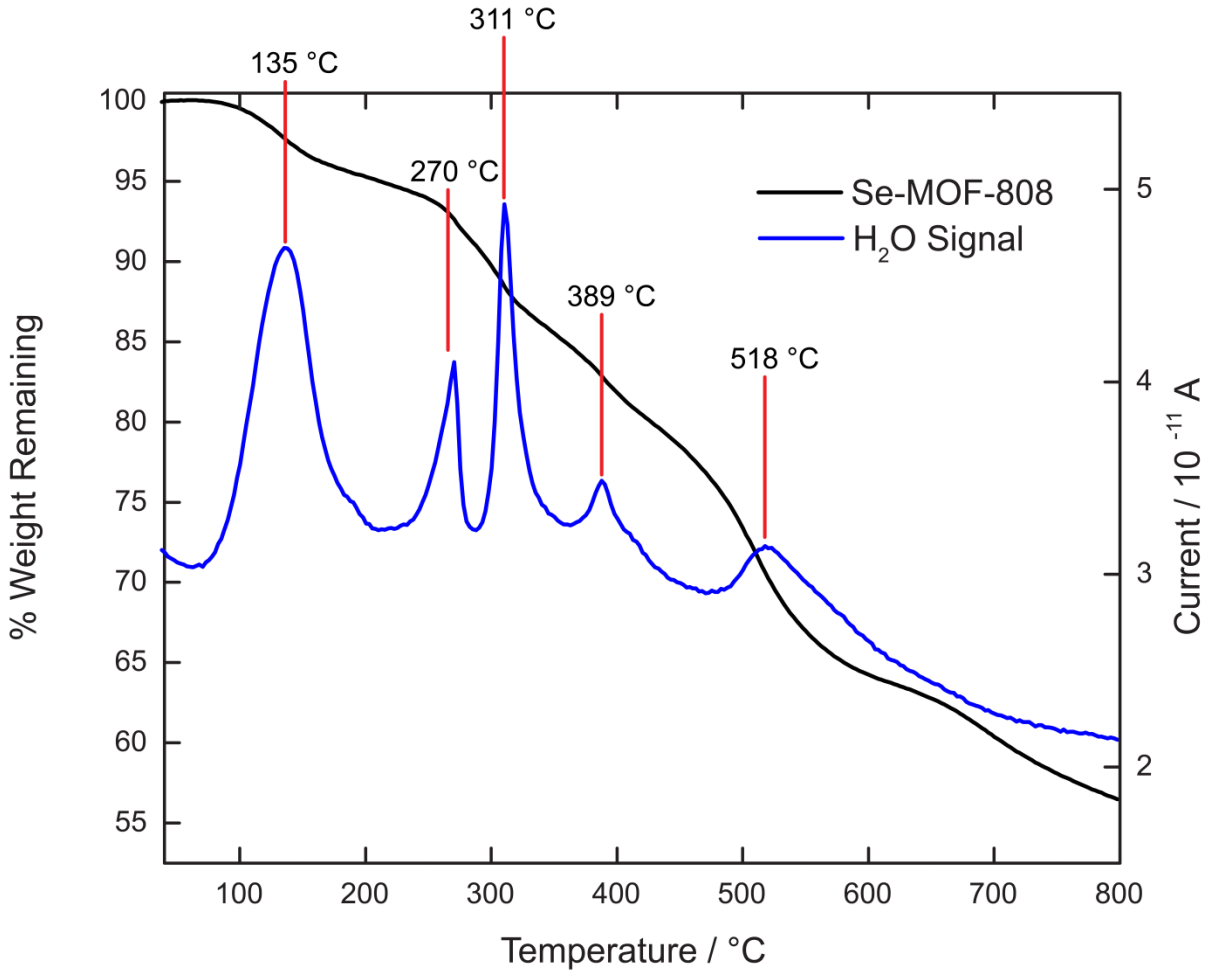

396

397 **Supplementary Figure 5.** TGA-MS plot of activated MOF-808-SeO_4 under argon atmosphere with the
398 thermogravimetric plot (black) and corresponding water loss signal (blue). The first mass loss, with the
399 water signal peaking at 135 °C, corresponds of water coordinated to the framework that is lost prior to full
400 structure decomposition beginning around 270 °C. The most credible explanation for the lower
401 temperature decomposition of MOF-808-SeO_4 compared to MOF-808-SO_4 is the much larger strain on
402 chelating selenate, since the former is distorted to a much greater degree compared with chelating sulfate.
403 Quantification of the water signals correspond to 2.9 water molecules per cluster for the first peak
404 centered at 135 °C.

405

406

407

Section 6: N_2 Sorption Isotherms

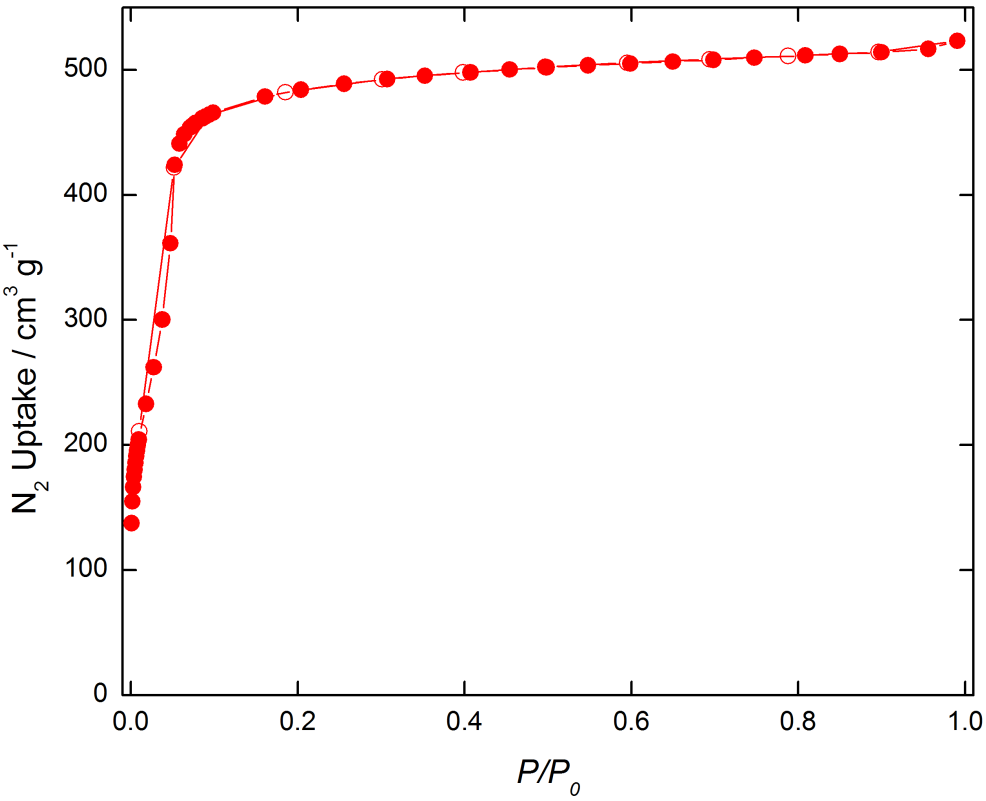

Supplementary Figure 6. N_2 adsorption isotherm of pristine MOF-808 at 77K.

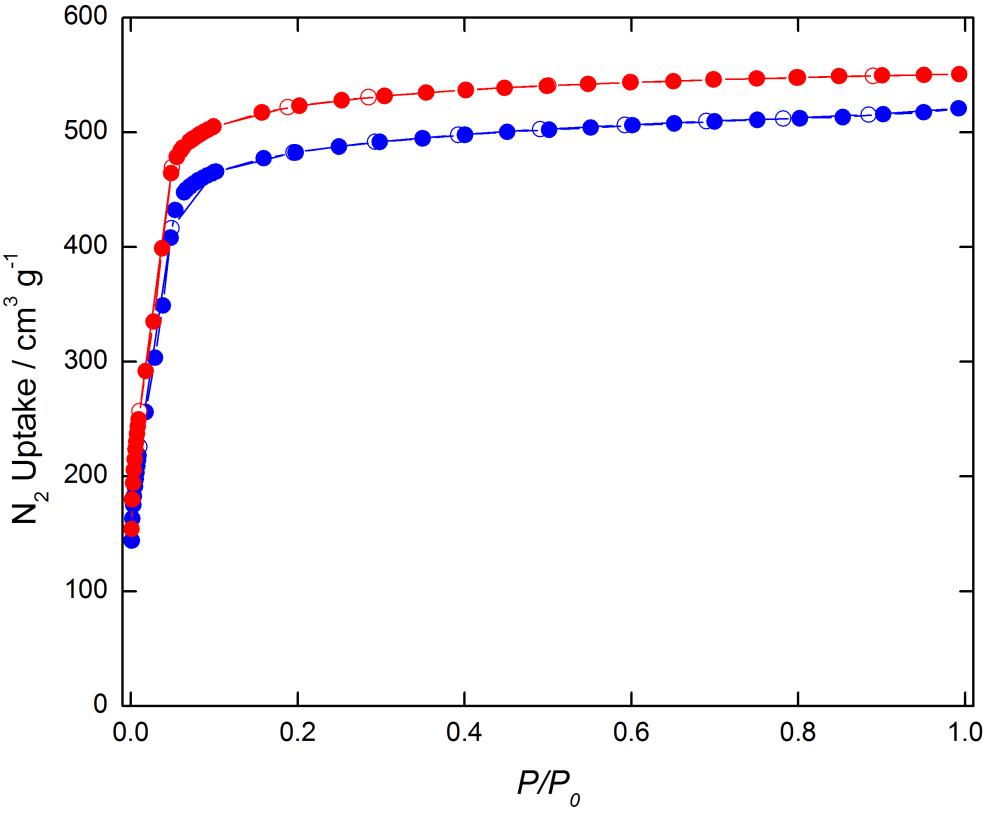

411

412 **Supplementary Figure 19.** N_2 adsorption isotherms of MOF-808-SO_4 (blue circles) and dehydrated
413 MOF-808-SO_4 (red circles) at 77K.

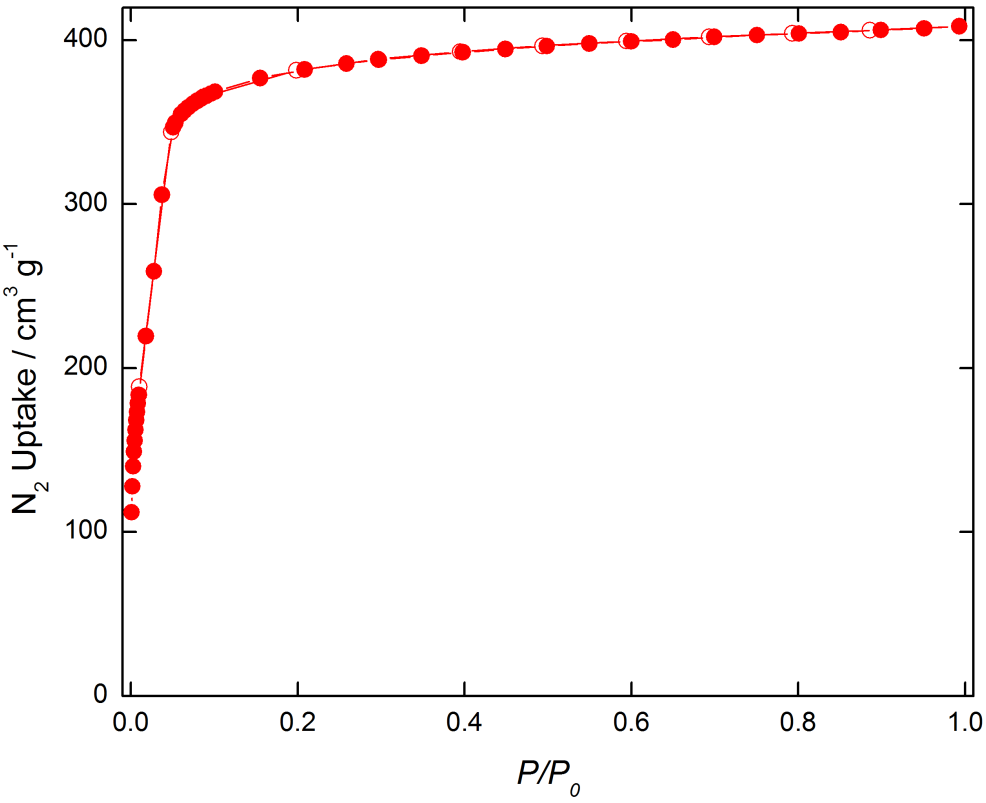

414

415 **Supplementary Figure 20.** N_2 adsorption isotherm of at 77K.

416

Section 7: Solid State NMR Spectroscopy

^{31}P Solid State NMR experiments. Samples for ^{31}P Solid State NMR were prepared following a slightly modified procedure based on the previously reported method (*4*). Briefly, around 100 mg MOF sample was activated as described in Section 1, and 1.5 mL of 0.2 M TMPO in chloroform was added and mixed with the MOF sample. This suspension was then evacuated under dynamic vacuum at room temperature overnight, then at 50 °C for 8 hours. The resulting solid was then packed into 75 uL Doty XC5 Kel-F sealing cells under argon atmosphere, and inserted into a Doty 5 mm thin-wall zirconia rotor with Kel-F turbine caps. Solid state NMR spectra were collected using a 7.05 T magnet with a Tecmag Discovery spectrometer operating at 300.13 MHz for 1H and 121.5 MHz for ^{31}P. ^{31}P chemical shifts were externally referenced to aqueous H_3PO_4 (85%) at 0 ppm. Experiments were performed on a Doty 5-mm triple resonance MAS probe operating in ^{1}H/^{31}P/^{87}Sr mode. Magic angle spinning (MAS) was used to collect high resolution NMR spectra at a spinning rate of 8 kHz. ^{31}P NMR experiments were performed with a ^{31}P 90° pulse time of 6 μs and a continuous wave ^{1}H decoupling B_1 field of 60 kHz. Spectra were collected with a recycle delay time of 11 s, and were processed with 5 Hz line broadening.

^{1}H Solid State NMR experiments. For direct ^{1}H MAS experiments, samples of MOF-808-SO_4 and dehydrated MOF-808-SO_4 were packed into Doty 5 mm thick-wall zirconia rotors with Kel-F turbine caps under argon atmosphere. Solid state NMR spectra were collected using a 7.05 T magnet with a Tecmag Apollo spectrometer operating at 300.27 MHz for ^{1}H. ^{1}H chemical shifts were externally referenced to TMS at 0 ppm. Experiments were performed on a Doty 5-mm triple resonance MAS probe. Magic angle spinning (MAS) was used to collect high resolution NMR spectra at a spinning rate of 6 kHz. Pulse-acquire ^{1}H NMR experiments were performed with a ^{1}H 90° pulse time of 4 μs and a recycle delay time of 5 s. The ^{1}H back-to-back (BABA) rotor-synchronized DQ recoupling experiment was run at 11.74 T field using a Bruker AV-500 spectrometer operating at 500.2 MHz for ^{1}H. The experiment was performed using a Bruker 4 mm CP-MAS probe at an MAS rate of 12.5 kHz, with a 4 μs ^{1}H 90° pulse time and recorded using two rotor period cycles with the BABA sequence for excitation and reconversion of the double quantum coherences. Spectra were processed without apodization.

The MOF-808-SO_4 system differs from typical organic molecular solids in that there is not a dense network of protons. The majority of proton-proton distances on a single zirconium cluster are greater than 2 Å, and distance between clusters imposed by the MOF framework reduces the influence of long-range homonuclear dipolar couplings. The spin interactions in this system thus approach the limit of isolated two-spin dipolar couplings, which can be easily resolved with magic-angle spinning (MAS) even at relatively low spinning rates.

^{1}H NMR Chemical shift calculations. The NMR chemical shielding tensors for the atoms in two of the DFT structure-optimized clusters were calculated using mPW1PW91 and the default gauge-independent atomic orbital (GIAO) method available in Gaussian 09 with the basis set 6-311++G(2d,2p) for all atom types excluding Zr, for which the basis lanl2dz, 5d, 7f was used (*7 - 9*). ^{1}H chemical shifts were referenced to tetramethylsilane, for which the structure and NMR shifts were calculated at the same level of theory. No scaling factor was applied to the ^{1}H chemical shifts, and as such we expect significant deviation from experimentally observed shifts; instead the relative magnitudes of, and differences between, the calculated shift values were used as a tool to inform the assignment of peaks in the experimental ^{1}H NMR results.

Exposure to atmospheric moisture (approximately 50% RH at 20 °C) also results in the loss of acidity as observed previously (4), meaning water is a key component in the acidic properties of MOF-808-SO_4, but not when it is in excess. This observation in MOF-808-SO_4 is consistent with the proposition that the acid catalysis of its analogue, sulfated zirconia, only operates in a specific humidity range (10). Supplementary figure 21 shows a ^{1}H NMR spectrum after exposure to atmospheric moisture. There is a broad resonance centered about 5.2 ppm which we assign as adsorbed water. The presence of this excess water should level the material's acidity to the acidity level of the hydronium ion. As the resonance of bulk water is 4.8 ppm, the slight upfield shift could be due to a lowering of the pH of the adsorbed water by some deprotonation of the active site. Several other new peaks are present in the spectrum of the hydrated MOF, which are likely protons in new hydroxide and adsorbed water species resulting from the introduction of water vapor, but it is difficult to assign them precisely.

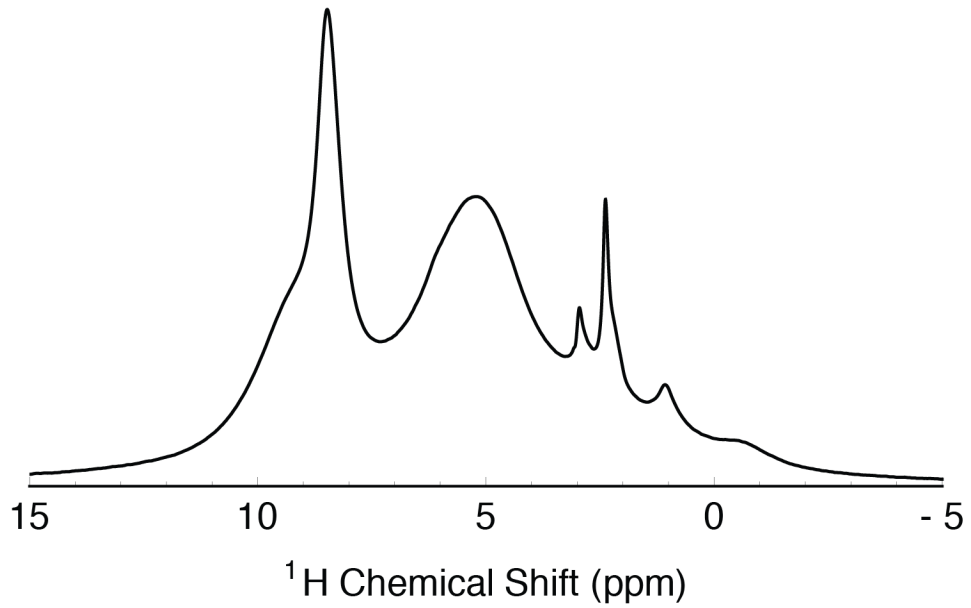

Supplementary Figure 21. Plot of the ^{1}H NMR spectra of MOF-808-SO_4 exposed to atmospheric moisture (approximately 50% RH at 20 °C).

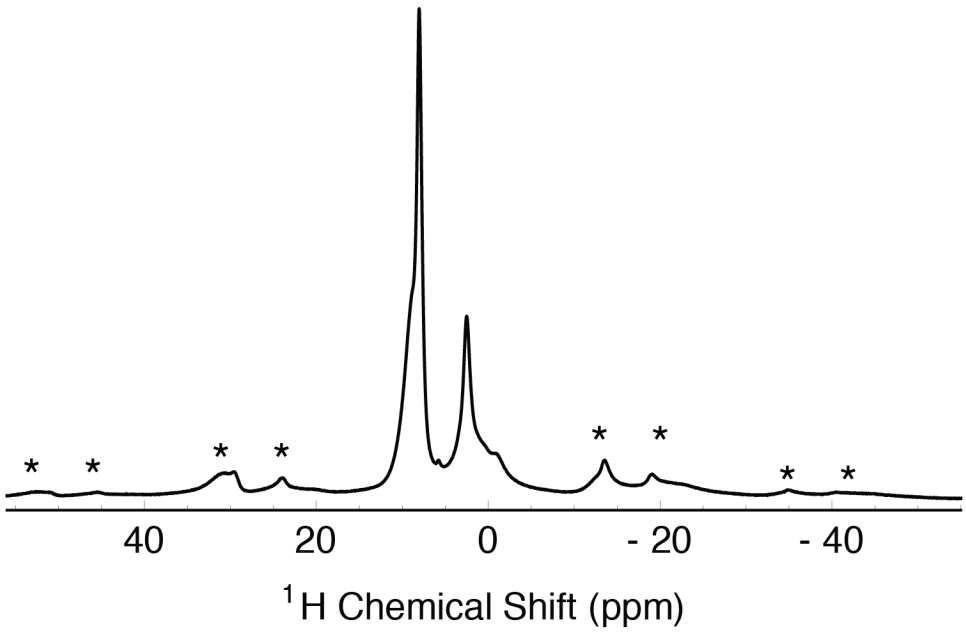

480

481 **Supplementary Figure 22.** Plot of the ^{1}H NMR spectra of MOF-808-SO_4 seen in main text figure
482 5a, but displayed with the frequency range extended to show the manifold of spinning sidebands
483 (denoted by asterisks).

484

485 **Supplementary Table 4.** Calculated ^{1}H NMR Chemical Shifts for '2wopp_optS,' a cluster model
486 with two chelating sulfates with adjacent water molecules

Atom Label	Chemical Group	Chemical Shift (ppm)	Notes
18	μ_3-OH	9.3889	H-bonded to a chelating SO_4
23	μ_1-OH	5.7650	Adjacent to H_2O but not H-bonded
26	μ_3-OH	5.1614	Isolated on cluster
34	μ_3-OH	2.8991	Enclosed between the three terminal acetates at the end of the cluster
52	μ_1-OH	7.1503	
53	μ_1-OH	6.2171	
54	H_2O	13.7517	Strongly H-bonded to a chelating SO_4, and SO_4 is H-bonded to 18, aka "H_a" in the acid site
74	H_2O	4.6606	On H_2O with 54, aka "H_b" in the acid site
79	H_2O	5.6023	On H_2O with 80, aka "H_b" in the

			acid site
80	H_2O	10.7284	Strongly H-bonded to a chelating SO_4, which itself has no H-bond to μ^3-OH, aka "H_a" in the acid site

Supplementary Table 5. Calculated ^{1}H NMR Chemical Shifts for '2opthighS,' a cluster model with one bridging and one chelating sulfate, and one adsorbed water molecule.

Atom Label	Chemical Group	Chemical Shift (ppm)	Notes
21	μ^3-OH	9.4348	H-bonded to chelating SO_4
26	μ^3-OH	10.0635	H-bonded to bridging SO_4
29	μ^1-OH	5.4765	
37	μ^3-OH	3.1569	Enclosed between the three terminal acetates at the end of the cluster
54	μ^1-OH	5.0904	
55	μ^1-OH	10.979	Partial H-bond to SO_4
76	H_2O	3.2215	On H_2O with 77
77	H_2O	5.2524	Adjacent to bridging SO_4

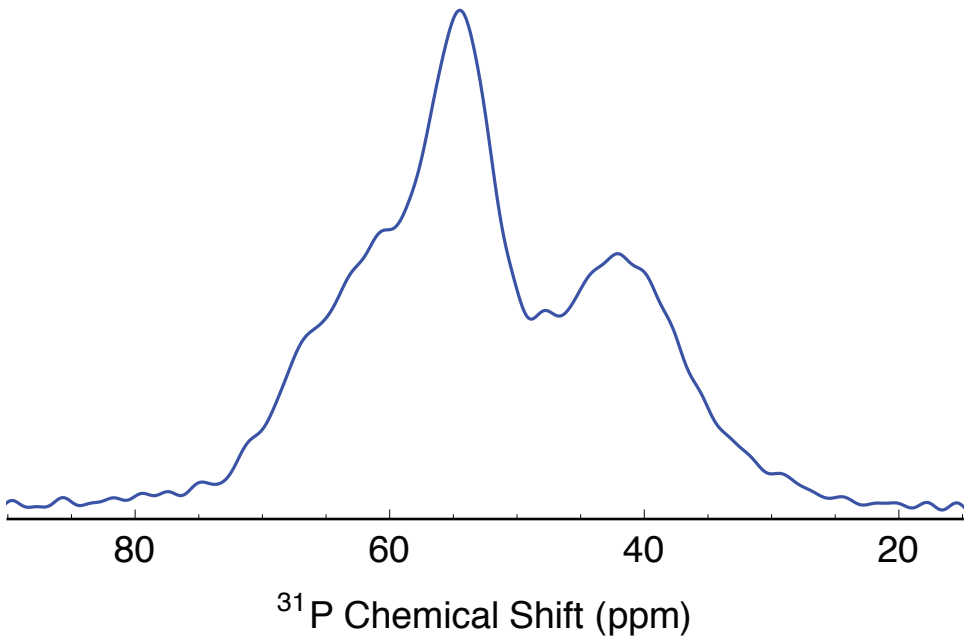

Supplementary Figure 23. Plot of the ^{31}P NMR spectra of trimethylphosphine oxide (TMPO) adsorbed into MOF-808-SeO_4. Though not as prominent as the peak at 69 ppm for MOF-808-SO_4 (Main text figure 3), there is signal intensity in the region of 60-70 ppm, suggesting the presence of strong acid sites in MOF-808-SeO_4. The peak centered at 42 ppm is due to excess TMPO that is not interacting with acid sites directly. Other peaks in the spectrum belong to TMPO adsorbed at various μ^1-OH, μ^3-OH, and water sites.

Section 8: Infrared Absorption Spectroscopy

Infrared (IR) absorption spectra of activated and dehydrated MOF samples were measured in transmission mode on a Thermo Scientific Nicolet 6700 FTIR spectrometer with a resolution of 1 cm^{-1}. The sample cell assembly process was performed in a N_2 glove box. A minute amount of the MOF powder sample was sandwiched between two CaF_2 windows to form a thin layer of 100 microns. The sample thickness was controlled by a Teflon spacer. Then the windows with the sample were assembled into a gas-tight IR sandwich sample cell to seal. After the assembly, the sample cell can be taken outside of the glove box without being compromised by moisture in air. The sample cell was then transferred to the measurement chamber of the FTIR spectrometer purged with CO_2-free dry air. The background spectrum was simply taken on the CO_2-free dry air for calculating the absorbance. Since the sample spectra were acquired in transmission mode on a powder sample, a large offset due to scattering is present in all the measurements.

Infrared spectroscopy of MOF-808-SO_4 before and after dehydration reveals changes in the region associated with O-H vibrations, where at least seven O-H stretches are observed in the spectral region of 3550-3800 cm^{-1} (Supplementary figures 24, 25). Prior to dehydration, there is a group of overlapping peaks in the range of 3550-3725 cm^{-1}, and two more distinct stretches located at 3737 and 3767 cm^{-1}. After dehydration, these two peaks at 3737 and 3767 cm^{-1} are no longer present, indicating that they originate from O-H vibrations belonging to adsorbed water. We assign the peaks in the range of 3550-3725 cm^{-1} as O-H vibrations belonging to various μ_3-OH and μ_1-OH groups. The strong blue shift of two O-H stretches at 3737 and 3767 cm^{-1} is characteristic of exposed hydroxyl groups not participating in hydrogen bonding (11, 12). One of these two peaks must belong to the O-H_b stretch in the acid site, while the other is likely an asymmetric stretching mode for terminal water not participating in a hydrogen bond to chelating sulfate. Our assignments are consistent with DFT calculations for the vibrational modes of our modeled clusters which were done using M06-L in Gaussian 09 with the basis set 6-31+G(d,p) for all atom types excluding Zr, for which the basis lanl2dz, 5d, 7f was used (9,13,14). The values for the O-H_b vibrational frequencies were calculated to be within 100-200 cm^{-1} of the peaks associated with O-H vibrations on water not participating in a hydrogen bond. However, the values for O-H_a vibrations were calculated to be present 1000-1500 cm^{-1} lower than the O-H_b vibrations. The O-H_a vibration should be located at a lower frequency due to the hydrogen bonding interaction with sulfate. However, no absorption features between 2000-3500 cm^{-1} were observed in the experiment that were not otherwise attributable to C-H modes on the BTC linker, due to a low signal to noise ratio (Supplementary figure 24b). We believe that the O-H_a vibration likely is not at such a low frequency as calculated by DFT, but rather may be present in the region between 3550-3725 cm^{-1}. However, due to the large degree of overlapping peaks in the region below 3700 cm^{-1}, it is difficult to see changes in this region after the water loss, but the presence of these blue-shifted O-H stretches and their subsequent loss after dehydration is consistent with our proposed Brønsted acid site.

Supplementary Table 6. Calculated IR frequencies for O-H vibrational modes in '2wopp_optS,' a cluster model with two chelating sulfates with adjacent water molecules.

Frequency (cm^{-1})	**Chemical Group primarily associated with the calculated vibrational mode**

3779	μ^1-OH
3747	μ^3-OH
3745	μ^1-OH
3718	μ^1-OH
3679	μ^3-OH
3657	O-H_b on H_2O for site 1
3588	O-H_b on H_2O for site 2
3220	μ^3-OH
2988	O-H_a on H_2O for site 2
2604	O-H_a on H_2O for site 1

Supplementary Table 7. Calculated ^{1}H NMR Chemical Shifts for '2opthighS,' a cluster model with one bridging and one chelating sulfate, and one adsorbed water molecule.

Frequency (cm^{-1})	**Chemical Group primarily associated with the calculated vibrational mode**
3824	μ^1-OH
3780	μ^3-OH
3766	μ^1-OH
3750	Asymmetric stretch H_2O
3532	μ^1-OH
3526	Symmetric stretch H_2O
3241	μ^3-OH
3223	μ^3-OH

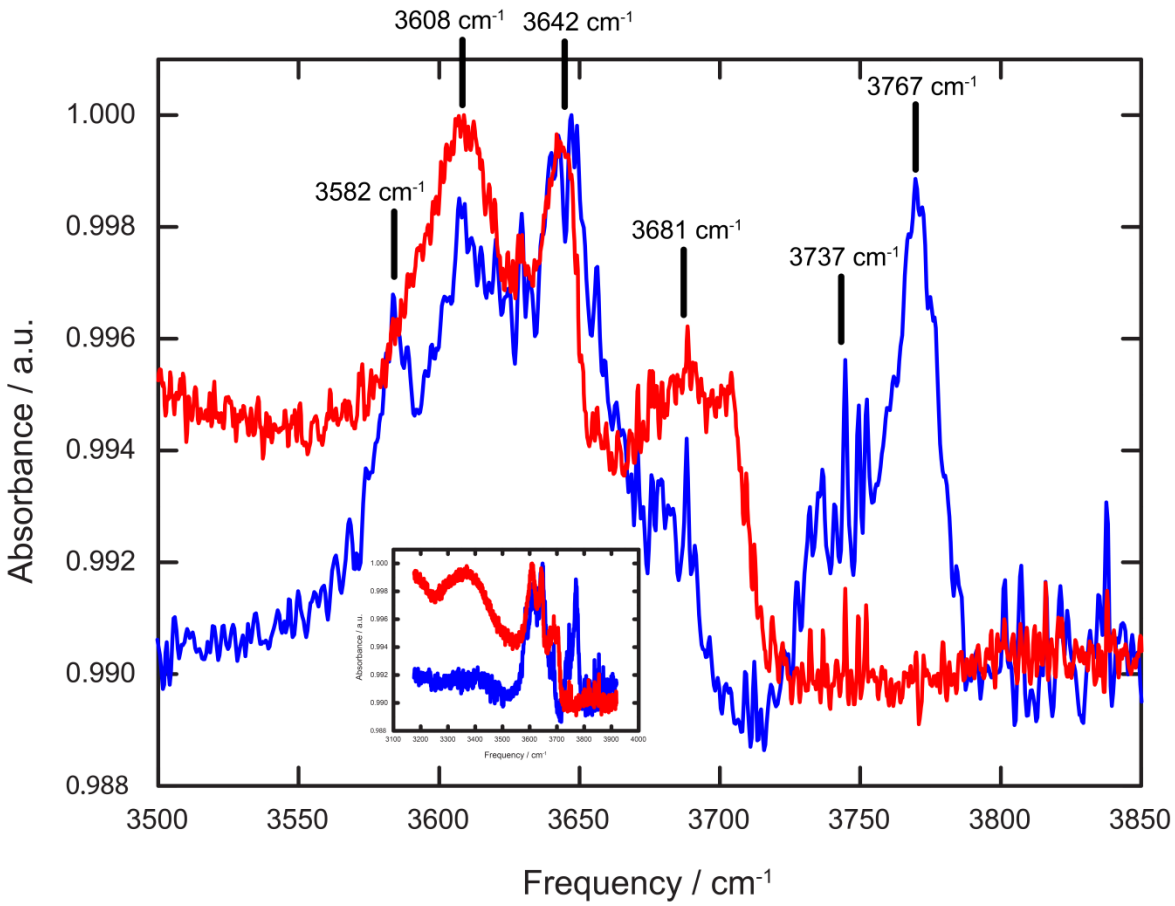

548

549 **Supplementary Figure 24a.** A comparison of the IR spectra of activated (blue) and dehydrated (red)
550 stages of MOF-808-SO_4 in the spectral region relevant to O-H stretches. The most notable feature is the
551 loss of the two blue-side peaks at 3737 and 3767 cm^{-1}. The inset is included to show the broad feature
552 centered around 3350 cm^{-1} in the dehydrated structure, which corresponds to a minute amount of water
553 adsorbed onto the MOF-808-SO_4 crystals.

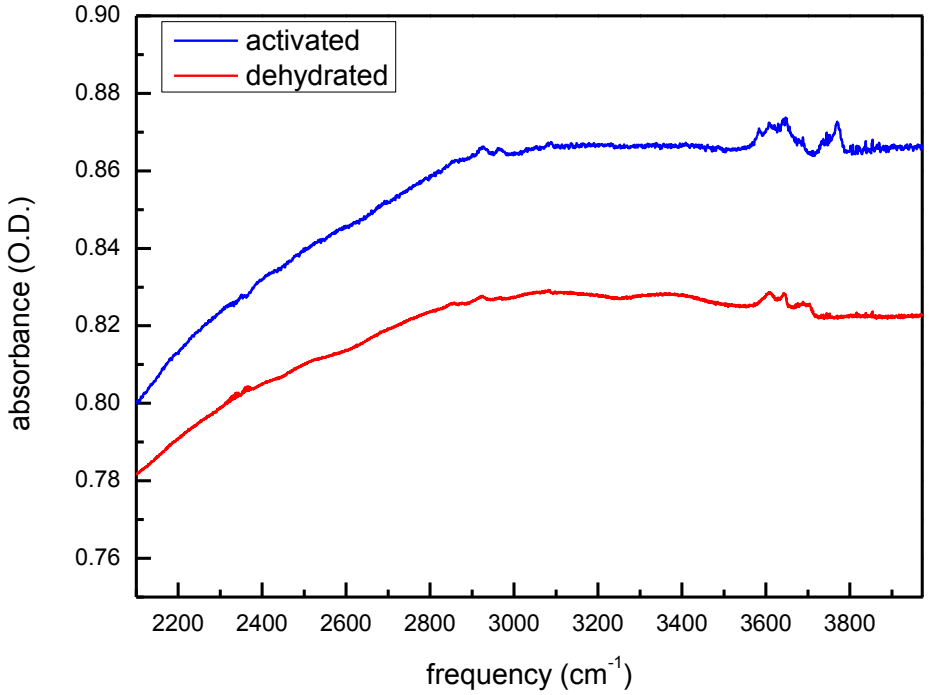

554

555 **Supplementary Figure 24b.** Expanded range IR spectra shown in supplementary figure 24a, showing the
556 lack of distinct features between 2000-3000 cm^{-1} that cannot otherwise be attributed to aromatic C-H
557 vibrational modes of the linker, and the low signal-to-noise in the region between 3000-4000 cm^{-1} that was
558 characteristic of our IR studies for multiple batches of this material.

559

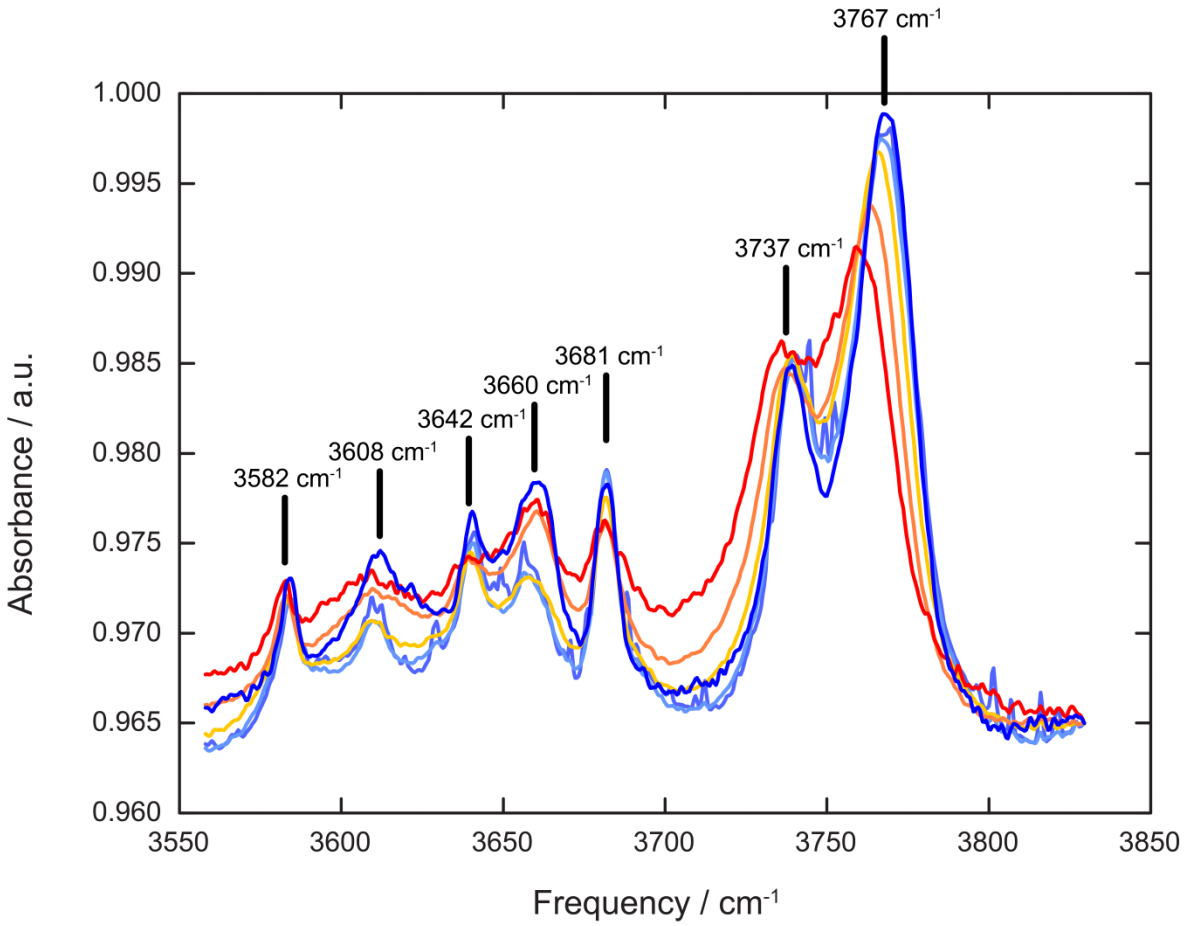

Supplementary Figure 25. A comparison of the IR spectra of a different batch (compared to supplementary figure 24) of activated MOF-808-SO_4 measured at different temperatures. Heating the sample broadens the peaks as the local environment becomes more disordered due to thermal motion. The process is reversible between room temperature and 200 °C. The measurement was started at room temperature (light blue) then heated gradually to 40 °C (light purple), 80 °C (yellow), 125 °C (orange), 200 °C (red), and cooled back down to room temperature (dark blue).

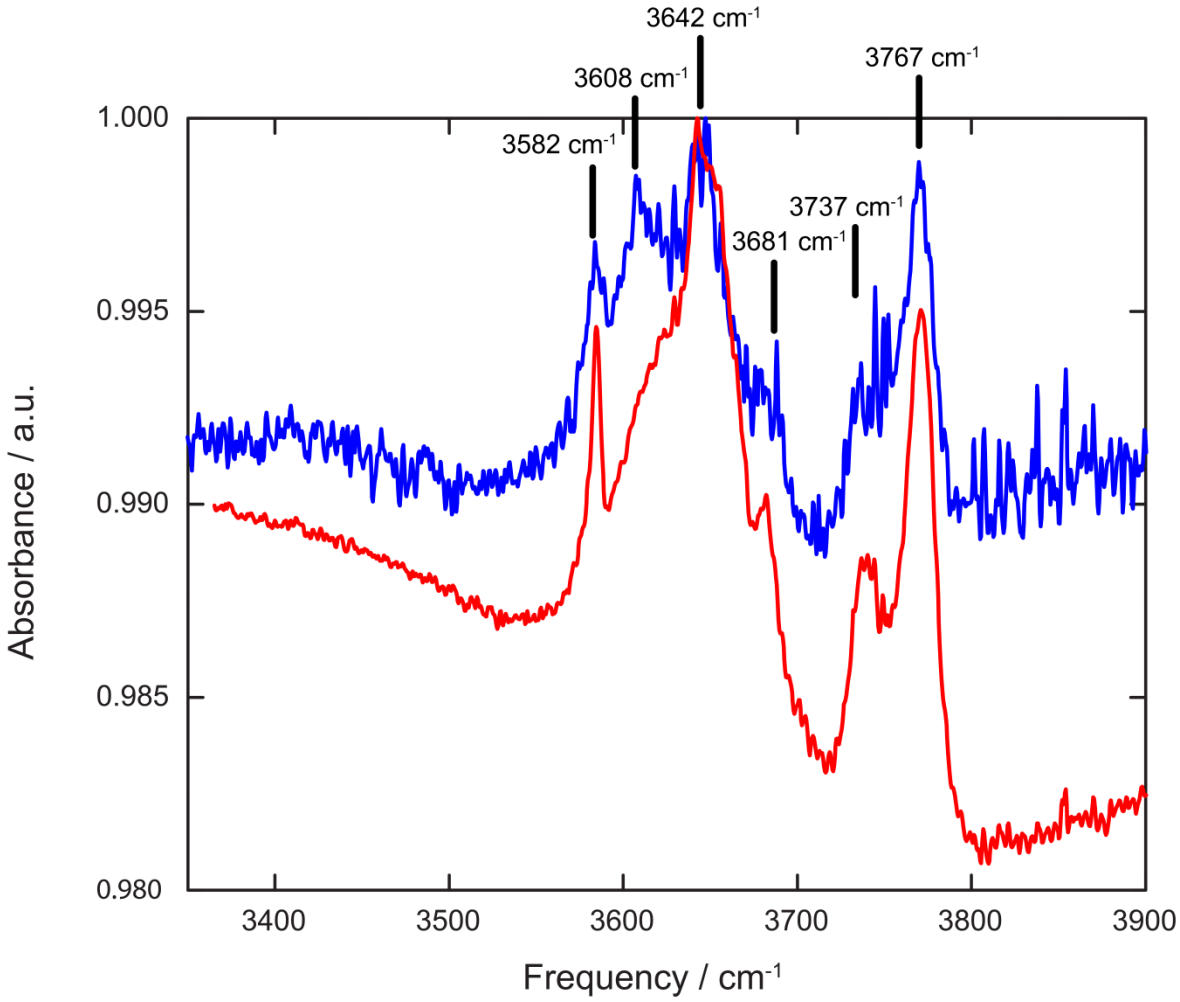

Supplementary Figure 26. A comparison of the *in situ* IR spectra of activated MOF-808-SO_4 (blue) and MOF-808-SeO_4 (red) in the energy region relevant to O-H stretches. Both samples display the same O-H stretch features, indicating the water and hydroxide environments in both samples are similar.

Section 9: Scanning Electron Microscopy

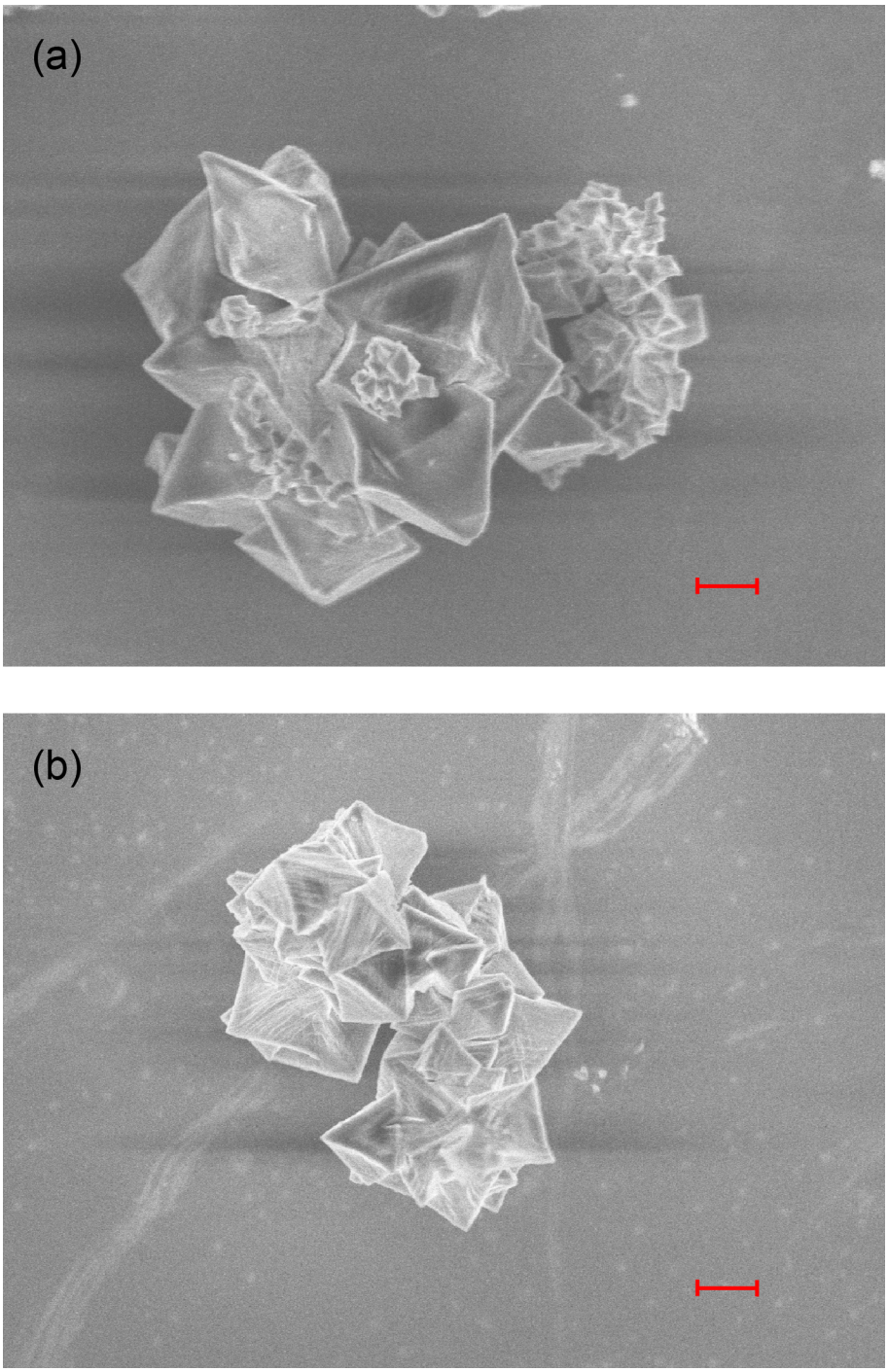

Supplementary Figure 27. Scanning electron microscope (SEM) images of (a) MOF-808-SO_4 and (b) MOF-808-SeO_4 following activation under dynamic vacuum at 120 °C (scale bar 1 μm).

Section 10: Cluster Geometry Optimization

Cluster optimizations were performed and geometrically optimized using density functional theory (DFT), based on the formula $Zr_6O_4(OH)_4(C_2H_3O_2)_6(SO_4)_2(OH)_2(OH_2)_x$, where x = 2 or 3. Acetate groups were used instead of BTC as a terminal ligand. The functional B97-D3 was chosen, which is the B97 functional with Grimme's dispersion term added on to account for dispersive effects that B97 misses. The chosen basis set was 6-31G* for all non-Zr atoms. For Zr, the CRENBL effective core potential was used for core electrons, with the matching CRENBL basis for valence electrons. A very fine grid consisting of 90 radial points and 590 angular points was selected for the numerical integration step to account for exchange-correlation. Early evaluation of cluster models by classical force field geometry optimization followed by energy calculation found that an uneven distribution of charge or chemical species resulted in much higher energy configurations, or even failed to converge. For instance, a configuration where two hydroxides are localized on one zirconium atom and two open metal sites are assigned to another was 300-400 kJ mol^{-1} higher in energy than both zirconium atoms assigned a single hydroxide group each, depending on the exact configuration.

Section 11: Acid Catalysis of Isobutene

A flow reactor set-up was used to test the catalytic performance of various acid catalysts: H-ZSM-5 (ammonium type, Si/Al ratio 20/1, Alfa Aesar), Amberlyst (Sigma Aldrich) and sulfated zirconia. Sulfated zirconia was prepared as explained in section 1. Gas feeds of 2 mL min^{-1} isobutene and 20 mL min^{-1} He regulated by a mass flow controller to be at 1 atm, were mixed together and directed towards the catalyst (90 mg), loaded into a tube furnace. The temperature of the catalyst bed was monitored by a K-type thermocouple controlled by a PID controller. The products were analyzed using an HP 6890 series GC-MS with a Supelco column (phase 23% SP-1700 support, 80/100 chromosorb PAW). Since the number of acid sites for each catalyst is unknown, the catalysts were compared by mass. The conversion and selectivity of isobutene and isooctene were calculated using the following equations:

$$\text{Isobutene conversion } (\%) = \frac{\text{Isobutene}_{in} - \text{Isobutene}_{out}}{\text{Isobutene}_{in}} \times 100$$

$$\text{Isooctene selectivity } (\%) = \frac{n\text{Isooctene}}{n\text{Dimers} + n\text{Trimers}} \times 100$$

where n is number of hydrocarbons in moles.

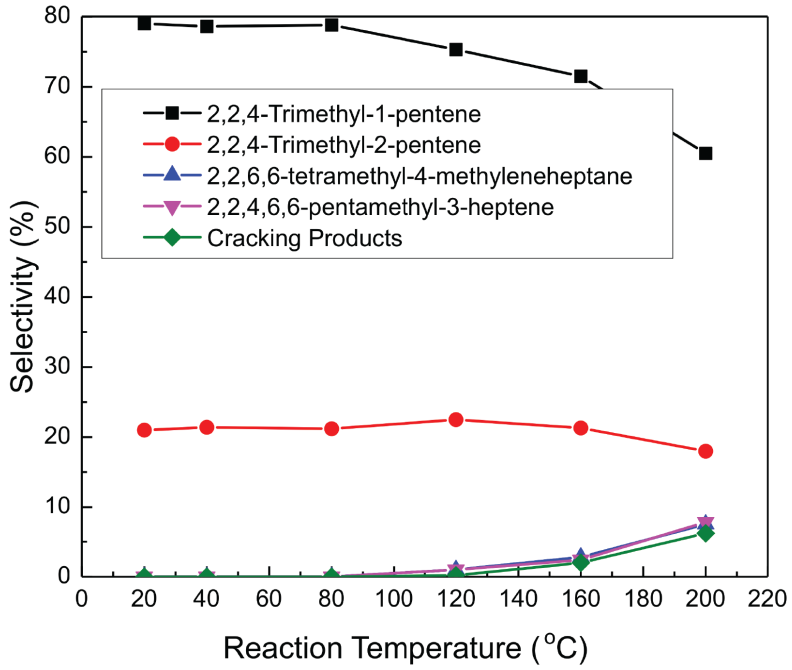

Supplementary Figure 28. Product distribution for the dimerization of isobutene using MOF-808-SO_4.

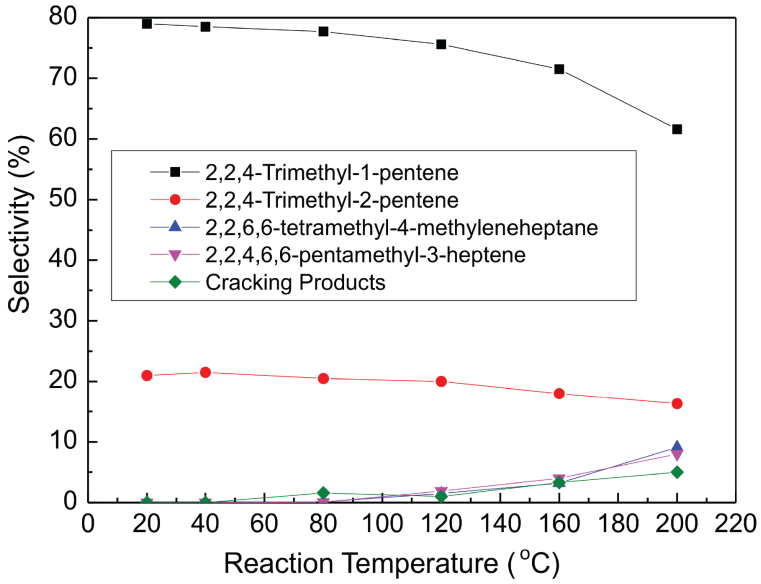

618

619 **Supplementary Figure 29.** Product distribution for the dimerization of isobutene using dehydrated
620 MOF-808-SO_4.

621

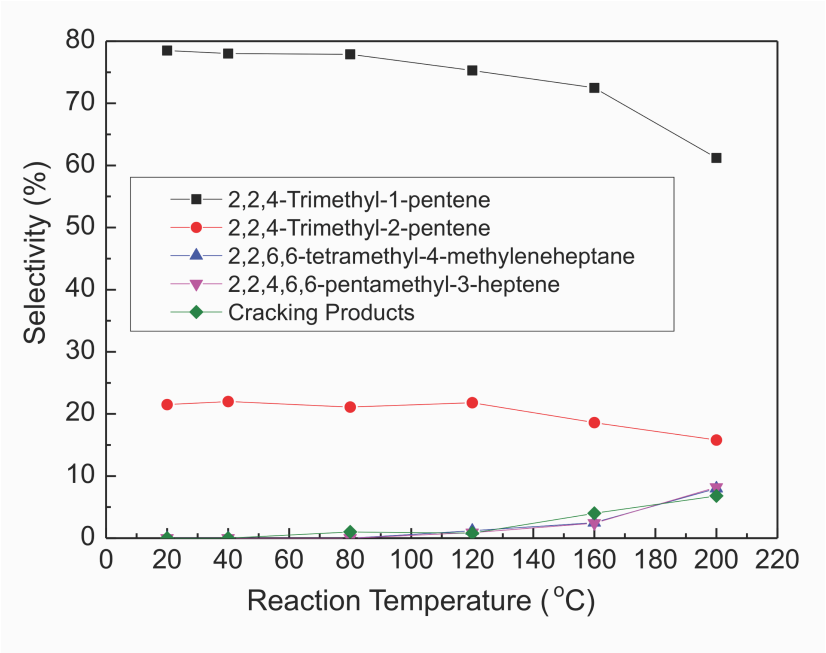

622

623 **Supplementary Figure 30.** Product distribution for the dimerization of isobutene using sulfated zirconia.

624

Section 12: References

1. Bruker, in *APEX2 (Bruker AXS Inc., Madison, Wisconsin, U.S.A)* (2010).

2. G. M. Sheldrick, A short history of SHELX. *Acta Crystallogr. Sect. A Found. Crystallogr.* **64**, 112–122 (2007).

3. O. V. Dolomanov, L. J. Bourhis, R. J. Gildea, J. A. K. Howard, H. Puschmann, OLEX2: A complete structure solution, refinement and analysis program. *J. Appl. Crystallogr.* **42**, 339–341 (2009).

4. J. Jiang *et al*., Superacidity in Sulfated Metal – Organic Framework-808. *J. Am. Chem. Soc.* **136**, 12844–12847 (2014).

5. X. Song and A. Sayari., Sulfated zirconia-based strong solid-acid catalysts: recent progress. *Catalysis Reviews* **38,** 329-412 (1996).

6. TOPAS 5. *Bruker AXS, Madison, WI, USA*.

7. R. Krishnan, J. S. Binkley, R. Seeger, J. A. Pople, Self-consistent molecular orbital methods. XX. A basis set for correlated wave functions. *J. Chem. Phys.* **72**, 650–654 (1980).

8. J. Struppe, Y. Zhang, S. Rozovsky, 77Se chemical shift tensor of L-selenocystine: Experimental NMR measurements and quantum chemical investigations of structural effects. *J. Phys. Chem. B.* **119**, 3643–3650 (2015).

9. Gaussian 09, Revision D.01, M. J. Frisch, G. W. Trucks, H. B. Schlegel, G. E. Scuseria, M. A. Robb, J. R. Cheeseman, G. Scalmani, V. Barone, G. A. Petersson, H. Nakatsuji, X. Li, M. Caricato, A. Marenich, J. Bloino, B. G. Janesko, R. Gomperts, B. Mennucci, H. P. Hratchian, J. V. Ortiz, A. F. Izmaylov, J. L. Sonnenberg, D. Williams-Young, F. Ding, F. Lipparini, F. Egidi, J. Goings, B. Peng, A. Petrone, T. Henderson, D. Ranasinghe, V. G. Zakrzewski, J. Gao, N. Rega, G. Zheng, W. Liang, M. Hada, M. Ehara, K. Toyota, R. Fukuda, J. Hasegawa, M. Ishida, T. Nakajima, Y. Honda, O. Kitao, H. Nakai, T. Vreven, K. Throssell, J. A. Montgomery, Jr., J. E. Peralta, F. Ogliaro, M. Bearpark, J. J. Heyd, E. Brothers, K. N. Kudin, V. N. Staroverov, T. Keith, R. Kobayashi, J. Normand, K. Raghavachari, A. Rendell, J. C. Burant, S. S. Iyengar, J. Tomasi, M. Cossi, J. M. Millam, M. Klene, C. Adamo, R. Cammi, J. W. Ochterski, R. L. Martin, K. Morokuma, O. Farkas, J. B. Foresman, and D. J. Fox, Gaussian, Inc., Wallingford CT, (2016).

10. D. Fraenkel, Acid Strength of Sulfated Zirconia Inferred from Catalytic Isobutane Conversion. *Chem. Lett.* **9**, 917–918 (1999).

11. E. Libowitzky, Correlation of O-H Stretching Frequencies and O-H-O Hydrogen Bond Lengths in Minerals. *Monatsh. Chem.* **130**, 104-115 (1999).

659 12. C. Yan, J. Nishida, R. Yuan, M.D. Fayer, Water of Hydration Dynamics in Minerals
660 Gypsum and Bassanite: Ultrafast 2D IR Spectroscopy of Rocks. *J. Am. Chem. Soc.* **138**,
661 9694-9703, (2016).

662 13. J.C. Howard, J.D. Enyard, G.S. Tschumper, Assessing the accuracy of some popular DFT
663 methods for computing harmonic vibrational frequencies of water clusters. *J. Chem. Phys.*
664 **143**, 214103, (2015).

665 14. I. M. Alecu, J. Zheng, Y. Zhao, and D. G. Truhlar, Computational Thermochemistry:
666 Scale Factor Databases and Scale Factors for Vibrational Frequencies Obtained from
667 Electronic Model Chemistries, *J. Chem. Theory Comput.* **6**, 2872-2887, (2010).